

Online Research @ Cardiff

This is an Open Access document downloaded from ORCA, Cardiff University's institutional repository: <https://orca.cardiff.ac.uk/id/eprint/146432/>

This is the author's version of a work that was submitted to / accepted for publication.

Citation for final published version:

Wang, Lei, Zhao, Xingyu, Wu, Zhangming ORCID: <https://orcid.org/0000-0001-7100-3282> and Chen, Wenpin 2022. Evidence theory-based reliability optimization for cross-scale topological structures with global stress, local displacement, and micro-manufacturing constraints. Structural and Multidisciplinary Optimization 65 (1) , 23. 10.1007/s00158-021-03112-w file

Publishers page: <http://dx.doi.org/10.1007/s00158-021-03112-w>
<<http://dx.doi.org/10.1007/s00158-021-03112-w>>

Please note:

Changes made as a result of publishing processes such as copy-editing, formatting and page numbers may not be reflected in this version. For the definitive version of this publication, please refer to the published source. You are advised to consult the publisher's version if you wish to cite this paper.

This version is being made available in accordance with publisher policies.

See

<http://orca.cf.ac.uk/policies.html> for usage policies. Copyright and moral rights for publications made available in ORCA are retained by the copyright holders.



Evidence Theory-based Reliability Optimization for Cross-scale Topological Structures with Global Stress, Local Displacement and Micro Manufacturing Constraints

Lei Wang^{a,b,c,1}, Xingyu Zhao^a, Zhangming Wu^b Wenpin Chen^d

a Institute of Solid Mechanics, School of Aeronautic Science and Engineering, Beihang University, Beijing 100083, China

b School of Engineering, Cardiff University, Newport Road 30-36, CF24 0DE, Cardiff, United Kingdom

c Aircraft and Propulsion Laboratory, Ningbo Institute of Technology, Beihang University, Ningbo 315100, China

d Shanghai Marine Equipment Research Institute, Shanghai 200031, P. R. China.

¹ Corresponding author: Lei Wang. Email: leiwang_beijing@buaa.edu.cn; ntucee.wanglei@gmail.com

ABSTRACT

An uncertainty-oriented cross-scale topology optimization model with global stress reliability constraint, local displacement constraint, and micro manufacturing control based on evidence theory is presented. The model is oriented to two-dimensional porous material structure, which concurrently designs the material distribution of both the macrostructure and the cell microstructure. During the optimization process, the homogenization method is used to solve the equivalent elastic modulus of the cell microstructure, which is then endowed to the macro elements for subsequent analysis. The local stress constraints are converted to a global constraint by P-norm to reduce the computational consumption. Considering the uncertainty factors, the evidence theory is utilized to process the uncertainty parameters and evaluate the reliability of the structural strength performance. Minimum length scale constraint is imposed on the cell microstructure by a density projection method for better manufacturability. Three numerical examples are presented to illustrate the availability of the proposed model.

Keywords: cross-scale topology optimization; global stress constraint; evidence theory; local displacement constraint; minimum length scale control

1 Introduction

Topology optimization is a structural optimization method that arranges the material distribution in the design domain. Bendsøe and Kikuchi [1] proposed the concept of topology optimization and a method of continuum structural topology optimization based on homogenization theory in 1988, which greatly stimulated the study of continuum structural topology optimization. After their work, topology optimization theory has made great progress and a series of optimization methods have been developed: Density-based Method [2-4], Evolutionary Structural Method [5, 6], and Level Set Method [7-10], etc.

Early topology optimization studies mainly focused on structural stiffness performance, while strength performance is rarely considered. In engineering practice, stress failure problems are widespread and have a great impact on structural safety. In recent years, topological optimization considering stress constraints has received more attention, and related problems are brought out. There are three main problems in stress-constrained topology optimization [11]: the phenomenon of singularity solution, the local nature of stress constraints, and the highly nonlinear stress behavior. The singularity phenomenon was discovered by Sved and Ginos [12] in the study of the three-bar truss subjected to three working conditions using mathematical programming. Cheng and Guo [13] pointed out that the essence of stress singularity is that the feasible design domain contains low-dimensional subdomains and proposed a ε relaxation method to obtain the global optimal solution. Rozvany and Sobieszczanski-Sobieski [14] proposed smooth envelope functions (SEF's) to eliminate the singularity problems encountered in rod structure optimization. Matteo [15] proposed the 'qp' method based on the ε relaxation method. The second problem is due to the local nature of the stress constraint: stress constraint should be imposed on every material point due to the difficulty in locating the maximum stress. A resolution to this problem is to replace the local stress constraints with an integrated stress constraint. Duysinx and Sigmund [16] utilized the P-norm format to fit the local stress constraints as a global constraint. Yang and Chen [17] proposed the KS function to integrate stress constraints, which has a fast convergence rate. Xia et al [18] utilize global stress and displacement constraints simultaneously to drive optimization. The third problem is that the stress constraints are highly non-linear dependent on the design: the stress is greatly affected by the change of density. Stress concentration is prone to occur in the holes and sharp corners of the structure, which will lead to the discontinuity of the stress constraint and brings difficulties in convergence. Therefore, the appearance of sharp features and intermediate density should be avoided to avoid divergence.

Multi-scale topology optimization generally refers to the topology optimization involving macro and micro scales, and the macrostructure can be regarded as an arrangement of microstructure. In the early 1990s, Sigmund [19] first conducted research on topology optimization of composite microstructure using the inverse homogenization method and achieved the optimal material layout design for the microstructure with Poisson's ratio between $[-1,1]$. After this work, scholars developed many multi-scale topology optimization design strategies around the material distribution and macroscopic arrangement of the cell microstructures. Multi-scale design based on the parameterized cell is the first strategy, which commonly selects the geometric parameters of the cell microstructure as design variables. In this field, scholars in recent years have carried out a number of works on parameter design based on preset cells [20-22] and attempt to expand the solution space by increasing the number of cell design parameters [23, 24]. The solution space of the parameterized cell is greatly affected by the initial configuration setting, which limits the performance of the cell microstructure sometimes. Multi-scale concurrent topology optimization is another strategy that can expand the design space to a greater extent by optimizing the topology design of cells at the micro level. However, multi-scale concurrent design inevitably faces large computational consumptions, so current researches mostly adopt the periodic arrangement of single cell microstructure or the macro design domain partition parallel design by finite species of cells. Such strategies combined with the homogenization method can greatly economize computing time. The main advantage of a globally uniform cell microstructure strategy is its low computational consumption, so it is widely used in some dynamic [25], uncertainty [26], and multidisciplinary [27, 28] topology optimization problems that involve large scale computations themselves. Compared with the globally uniform cell design, the multi-scale partition parallel design contains a larger design space. The main problem of this strategy is how to effectively and reasonably partition the macro design domain. Scholars have proposed methods such as partitioning by the macro density distribution [29, 30] and using the principal stress direction for partitioning [31], etc. The multi-scale topology optimization in this paper involves reliability constraints and microstructure length scale control. The globally uniform cells with periodic arrangement are utilized since the optimization problem itself involves large computational consumptions.

Reliability topology optimization considers uncertain factors and has developed theories such as probability reliability, fuzzy reliability, and non-probability reliability. The probabilistic reliability research is the most mature reliability theory, while the non-probabilistic reliability research started late[32-34]. The process of uncertainty information is the focus of reliability

problems. Evidence theory proposed by Dempster [35] and Shafer [36] can process the uncertainty information more objectively and comprehensively and has broad application prospects in reliability topology optimization. Agarwal et al [37] conducted reliability optimization based on evidence theory to solve multidisciplinary design problems. Bae et al [38] used evidence theory to quantify the uncertainty factors encountered in mechanical engineering and conducted an uncertainty optimization design of the aircraft wing part. Mourelatos and Zhou [39] proposed evidence-based design optimization (EBDO) and applied it to the optimization design of cantilever beams and internal pressure vessels. Vasile [40] applied evidence theory to the non-probabilistic reliability optimization design of Mercury and Mars rovers and obtained optimization results with good robustness. However, researches on continuum topology optimization based on evidence theory are relatively rare, and most of the existing researches is focused on discrete topology optimization.

With the development of additive manufacturing, processing porous materials with complex microstructure has become convenient. Considering the limited processing precision, it is necessary to impose length scale control on the cell microstructure in cross-scale topology optimization. In early studies, some impose constraints on density distribution to control length scale [41, 42]. In later works, the minimum length scale control method based on the Heaviside projection became a popular field [43-45]. In addition to the minimum length scale control, Zhang et al [46] proposed a length scale control method based on structural skeletons, which achieved the maximum and minimum length scale control by adding global constraints. Amir et al [47] constrained the structural stress by applying length scale control, and finally obtained design results that satisfy the stress and length scale constraints. The level set method has the advantage of clear topological boundaries, and some scholars [48-50] have proposed a series of length scale description functions based on this characteristic.

In this paper, a tentative study on the combination of evidence theory-based strength reliability, microstructure length scale control, and double-scale continuum topology optimization is carried out. The originality of this study is mainly reflected in the combination of evidence theory-based reliability assessment and gradient algorithm, double-scale sensitivity analysis, and simplified computational consumption of the optimization process. The remainder of this paper is organized as follows. In Section 2, the formulation of cross-scale topology optimization with global stress constraint is introduced. The basic conceptions of the evidence theory and structural reliability analysis based on the evidence theory are presented in Section 3. In Section 4, details of reliability constraint, length scale control method, and sensitivity analysis are introduced. The optimization procedure and some discussions on computational

consumption are demonstrated in Section 5. Three numerical examples are listed in Section 6 to demonstrate the effect of the proposed method.

2 General problem statements

Traditional stress-constrained optimal formulation based on finite element method can be depicted as

$$\begin{aligned}
 \min_{P_j} : \bar{V} &= \frac{\sum_{i=1}^N P_i \cdot V_i}{V}, \\
 i &= 1, 2, 3, \dots, N \\
 s.t. : \mathbf{KU} &= \mathbf{F} \\
 \sigma_{vM,k} &\leq \sigma_{cons}, k = 1, 2, \dots, M \\
 0 < \delta &\leq P_i \leq 1
 \end{aligned} \tag{1}$$

where P_i is the density design variable of the i -th element, V_i is the volume of the i -th element, V is the volume of the design domain, N is the number of the design variables, \mathbf{K} is the finite element global stiffness matrix, \mathbf{U} is the displacement response column vector, \mathbf{F} is the load column vector, $\sigma_{vM,k}$ is the von Mises stress of the k -th constraint point, σ_{cons} is the value of the stress constraint, M is the number of the stress constraints, δ is a small number set to avoid the singularity of the stiffness matrix. Since the von Mises is not uniform within the element, the von Mises stresses at the Gaussian points are often selected as the von Mises stresses of the element. In this paper, the arithmetic mean value of von Mises stresses at four Gaussian points $\left(\frac{1}{\sqrt{3}}, \frac{1}{\sqrt{3}}\right)$, $\left(-\frac{1}{\sqrt{3}}, \frac{1}{\sqrt{3}}\right)$, $\left(\frac{1}{\sqrt{3}}, -\frac{1}{\sqrt{3}}\right)$, and $\left(-\frac{1}{\sqrt{3}}, -\frac{1}{\sqrt{3}}\right)$ under the local coordinate is selected as the von Mises stress of the element as shown in Fig 1.

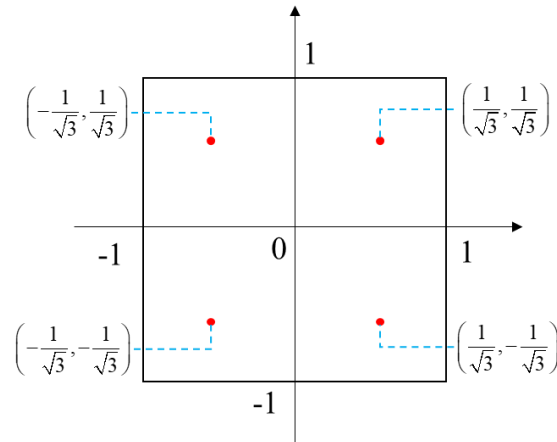


Fig 1 The Gaussian points under the local coordinate

In continuum structure topology optimization, the structure formed during the iteration

can't be accurately predicted, which brings difficulty in locating the position of maximum stress. If stress constraint is imposed on every element, it will lead to excessive computational consumption. A general treatment is to condense the stress constraints into a global constraint, i.e., select the maximum stress as the constraint:

$$\max(\sigma_{vM,k}) \leq \sigma_{cons} \quad (2)$$

Since $\max(\sigma_{vM,k})$ is a non-differentiable function, it can be smoothed by P-norm:

$$\sigma_{P-norm} = \left(\sum_{k=1}^N \sigma_{vM,k}^q \right)^{\frac{1}{q}} \quad (3)$$

where q controls the smoothness of the function. A large value of q will lead to a better approximation effect, but an excessive value will cause oscillation problems during iteration, so an improved function [51] is used:

$$\sigma_{PN} = c \cdot \sigma_{P-norm} = c \left(\sum_{k=1}^N \sigma_{vM,k}^q \right)^{\frac{1}{q}} \quad (4)$$

where the parameter c will be updated during each iteration by

$$c^I = a^I \frac{(\sigma_{vM,k})_{\max}^{I-1}}{\sigma_{PN}^{I-1}} + (1-a^I) c^{I-1} \quad (5)$$

The above parameter $a^I \in (0,1]$ controls the variations between c^{I-1} and c^I : $a^I \in (0,1)$ is chosen when c tends to oscillate, otherwise $\chi^I=1$ is chosen.

The objective of this paper is cross-scale topology optimization involving macrostructure and cell microstructure, thus the optimization model contains the macro and the micro design domains. Combined with the forenamed stress cohesion method, the formulation of stress-constrained cross-scale topology optimization can be expressed as

$$\begin{aligned} \min_{\rho_i, P_j} : \bar{V} &= \frac{\sum_{i=1}^N P_i \cdot V_i \cdot \frac{\sum_{j=1}^n \rho_j}{n}}{V}, \\ &i = 1, 2, 3, \dots, N, j = 1, 2, 3, \dots, n \\ s.t. : \mathbf{K}(\mathbf{D}_{Mac}) \cdot \mathbf{U} &= \mathbf{F} \\ \mathbf{D}_{Mac,i} &= P_i^\alpha \cdot \mathbf{D}_H, \mathbf{D}_{Mic,j} = \rho_j^\alpha \cdot \mathbf{D}_0 \\ \sigma_{PN} &\leq \sigma_{cons} \\ 0 < \delta &\leq P_i \leq 1, 0 < \delta \leq \rho_j \leq 1 \end{aligned} \quad (6)$$

where ρ_j is the density design variable of the j -th element in the micro design domain, n

is the number of micro design variables, $\mathbf{D}_{Mac,i}$ is the elastic matrix of the i -th element in the macro design domain, $\mathbf{D}_{Mic,j}$ is the elastic matrix of the j -th element in the micro design domain, $\mathbf{D}_{Mac,i}$ and $\mathbf{D}_{Mic,j}$ are processed by SIMP [52-54] method respectively to suppress the appearance of elements with intermediate density, \mathbf{D}_H is the equivalent elastic matrix of the cell microstructure, \mathbf{D}_0 is the elastic matrix of the material. The schematic diagram of the cross-scale topology optimization has been shown in Fig 2. It is worth noting that the microstructure can be macro-spatially varying, that is, each macro element corresponds to a unique microstructure. Considering the efficiency of the solution, the optimization in this paper adopts a globally uniform periodic arrangement microstructure design. The equivalent elastic matrix \mathbf{D}_H can be solved by the homogenization theory [55], which can obtain the equivalent elastic property of the cell microstructure by solving the response of the cell under periodic boundary conditions. The homogenization theory assumes that the microstructure has periodic repeating characteristics, and some macroscopic physical quantities can be depicted as micro-periodic functions such as

$$\begin{aligned} H_{ijkl}(\chi) &= H_{ijkl}(\chi, \gamma) = H_{ijkl}(\chi, \gamma + Y), \quad \gamma = \chi/b \\ u(\chi) &= u(\chi, \gamma), \quad \gamma = \chi/b \end{aligned} \quad (7)$$

where H_{ijkl} denotes the components of the elastic tensor ($i, j, k, l \in \{1, 2, 3\}$ for 3D; $\{1, 2\}$ for 2D), χ and γ denote the macro and micro coordinates respectively, Y is the period of the microscopic coordinates, b is a small number, u denotes the structural displacement field. Through the asymptotic expansion of u with respect to b and the linearized small perturbation hypothesis, combined with the displacement variation equation, the general expression of the equivalent tensor solved by the homogenization can be depicted as

$$H_{ijkl}^H = \frac{1}{|Y^\varepsilon|} \int_{Y^\varepsilon} \left(H_{ijkl} - H_{ijmn} \frac{\partial \psi_m^{kl}}{\partial \gamma_n} \right) dY^\varepsilon \quad (8)$$

where Y^ε is the periodic cell domain, H_{ijkl} denotes the components of the elastic tensor of the material, ψ_m^{kl} is the feature displacement, γ_n denotes the micro coordinate ($i, j, k, l, m, n \in \{1, 2, 3\}$ for 3D; $\{1, 2\}$ for 2D). The feature displacement ψ_m^{kl} can be solved by imposing unit strain fields under periodic boundary conditions. During the process of optimization, the equivalent elastic matrix serves as a link between two design domains: the macro structural response is solved by the macro elements endowed with the equivalent elastic

matrix, and the update of the cell microstructure is based on the macro structural response. The micro and macro scales obey the constitutive relationship of isotropic materials and anisotropic materials, respectively. Therefore, the constitutive equations of the two scales are

$$\begin{aligned} \text{micro} : \sigma_{ij} &= \lambda \theta \delta_{ij} + 2\mu \varepsilon_{ij} \\ \text{macro} : \sigma_{ij} &= H_{ijkl} \varepsilon_{ij} \end{aligned} \quad (9)$$

where σ_{ij} is the stress tensor, ε_{ij} is the strain tensor, δ_{ij} is Kronecker function, λ and μ are Lamé constants, θ is the volume strain.

Benefited from the homogenization processing, the equivalent macroscopic elastic properties of the cell microstructure can be transferred directly to the macro elements. Utilizing gradient algorithm and sensitivity, the density design variables of the two design domains can be updated simultaneously during the optimization iteration, so the double-scale optimization described in Eq.(6) can be carried out simultaneously at two scales instead of a nested optimization.

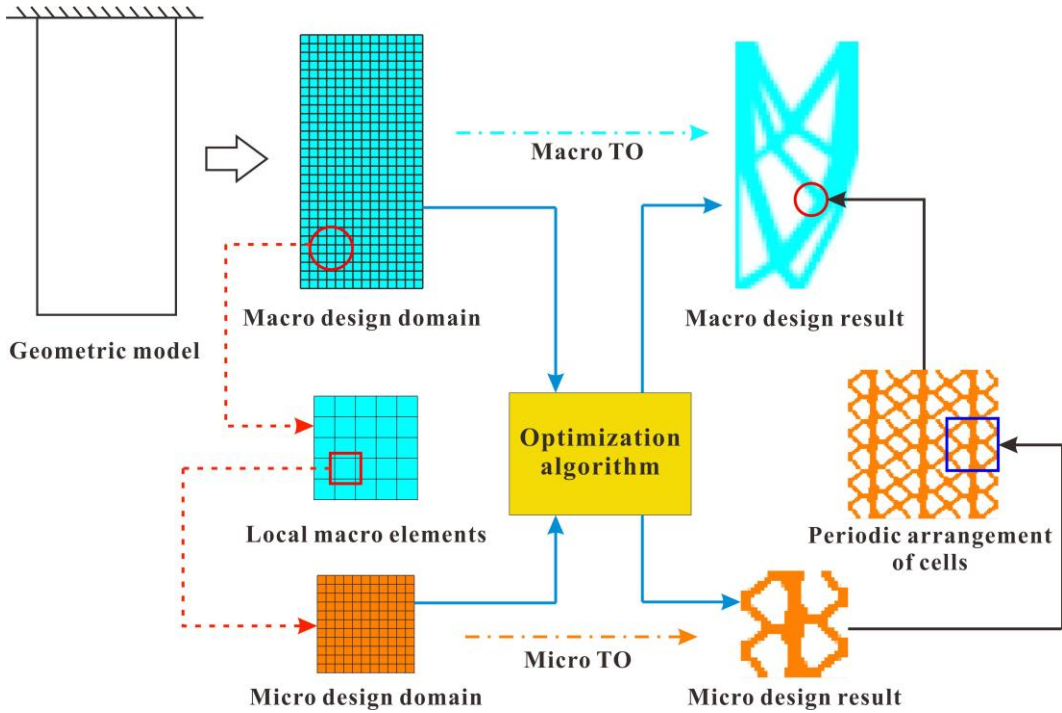


Fig 2 Double-scale topology optimization

3 Structural reliability analysis based on the evidence theory

Uncertain factors are widespread, and sometimes it is difficult to make accurate statistics on uncertainty information or obtain a sufficient number of samples. In this case, the non-probability reliability theory and the evidence theory are more applicable. Evidence theory is a generalization of classical probability theory, which uses basic probability assignment to

describe the inaccuracy and incompleteness of data. Compared with other uncertainty theories, evidence theory is a more general uncertainty modeling theory, which can effectively deal with random uncertainties, fuzzy uncertainties, and interval uncertainties. The principle of processing the uncertainty information and structural failure analysis based on the evidence theory will be discussed in this chapter.

3.1 Basic conceptions of evidence theory

Evidence theory is a theory of uncertainty induce and decision-making based on the framework of discernment, which contains basic probability assignment, belief function, plausibility function, and other elements. The framework of discernment is defined as a set that contains all the possible results of a problem, which is generally expressed by a non-empty set Θ . The set of all possible sub-propositions in the framework of discernment Θ is called the power set, which is denoted as 2^Θ . For example, the power set of the framework of discernment $\Theta = \{Y_1, Y_2, Y_3\}$ is

$$2^\Theta = \{\emptyset, \{Y_1\}, \{Y_2\}, \{Y_3\}, \{Y_1, Y_2\}, \{Y_1, Y_3\}, \{Y_2, Y_3\}, \{Y_1, Y_2, Y_3\}\} \quad (10)$$

Basic probability assignment (BPA) characterizes the reliability of arbitrary propositions, which is a projection from 2^Θ to the range $[0,1]$ satisfying

$$\begin{cases} m(A) \geq 0 \text{ for any } A \in 2^\Theta \\ m(\emptyset) = 0 \\ \sum_{A \in 2^\Theta} m(A) = 1 \end{cases} \quad (11)$$

When a set A satisfies $m(A) > 0$, it is called a focal element. The definition of basic probability assignment reflects the nature that the reliability of the empty set is 0 and the total reliability of all propositions is 1.

Evidence theory uses belief and plausibility to express the true degree of the proposition. For the set A , its belief function and plausibility function are

$$\begin{aligned} \text{Bel}(A) &= \sum_{B \subseteq A} m(B) \\ \text{Pl}(A) &= \sum_{B \cap A \neq \emptyset} m(B) \end{aligned} \quad (12)$$

$\text{Bel}(A)$ is the sum of the basic probability assignment of the evidence supporting A , which represents the lower bound of the probability when A occurs. $\text{Pl}(A)$ is the sum of the basic probability assignment of the evidence that partially and completely supports A , which

represents the upper bound of the probability when A occurs.

When there exists information from different sources or theories proposed by multiple experts, evidence synthesis rules can be used to fuse them into a more accurate and reliable form. Dempster rule is the most typical evidence synthesis rule, which supposes m_1, m_2, \dots, m_n is the basic probability assignment from multiple experts or multiple data sources under the same framework of discernment. Then the multi-source synthesis basic probability assignment of A is assigned as

$$m(A) = \frac{\sum_{\cap A_i = A} \prod_{1 \leq i \leq N} m_i(A_i)}{1 - K}, A \neq \emptyset \quad (13)$$

in which $K = \sum_{\cap A_i = \emptyset} \prod_{1 \leq i \leq N} m_i(A_i)$ denotes the conflict coefficient: $K = 0$ means no conflict

while $K = 1$ denotes a high degree of conflict. The Dempster rule is mainly used in cases where the conflict of evidence is small, and the cases of high conflict can be synthesized by other methods.

3.2 Analysis of structural failure based on evidence theory

In this section, the quantification and propagation analysis of uncertainty factors in structural parameters is carried out, and the structural failure probability is calculated based on evidence theory.

Consider the structural response under specified external load and boundary conditions:

$$\varphi = f(\boldsymbol{\theta}) \quad (14)$$

where $\boldsymbol{\theta} = [\theta_1, \theta_2, \dots, \theta_n]$ is the vector of the uncertainty parameters. The uncertainty parameter θ_j often satisfies some certain arrangement on its distribution interval $[\underline{\theta}_j, \bar{\theta}_j]$. According to the respective distributions of each uncertainty parameter, $[\underline{\theta}_j, \bar{\theta}_j]$ can be divided into n_j sub-intervals. The sub-intervals can then be combined to obtain the joint framework of discernment (FOD) C including all combinations:

$$C = \theta_1 \times \theta_2 \times \dots \times \theta_n = \left\{ c_k = [\theta_1^k, \theta_2^k, \dots, \theta_n^k] \mid \theta_j^k \in [\underline{\theta}_j, \bar{\theta}_j] \right\} \quad (15)$$

If the uncertainty parameters are independent of each other, the basic probability assignment of the focal element c_k can be expressed by

$$m(c_k) = m(\theta_1^k) m(\theta_2^k) \dots m(\theta_n^k) \quad (16)$$

Utilizing the structural failure domain $\kappa\{\varphi | g(\varphi) < 0, c_k \in C\}$ ($g(\varphi)$ is the structural response failure judgment function which is commonly referred to as performance function in reliability theory, $g(\varphi) < 0$ indicates structural failure), the belief function and the plausibility function can be calculated by

$$\text{Bel}(\kappa) = \sum_{c_k \subseteq \kappa} m(c_k), \quad \text{Pl}(\kappa) = \sum_{c_k \cap \kappa \neq \emptyset} m(c_k) \quad (17)$$

Now consider the optimization model mentioned in chapter 2. When considering uncertainty factors, it is reliable to restrict the upper bound of the stress response, but this will lead to a conservative design. Therefore, the structural failure probability can be used to judge structural failure more reasonably. Suppose the uncertainty variables are elastic modulus $E = [e_1, e_2, \dots, e_{n_1}]$ and external load $F = [f_1, f_2, \dots, f_{n_2}]$, where e_i and f_j are the subintervals of E and F . The joint framework of discernment of E and F can be expressed as

$$C = E \times F = \{c_k = [e_i, f_j] | e_i \in E, f_j \in F\} \quad (18)$$

Since E and F are independent of each other, the basic probability assignment of c_k can be calculated by

$$m(c_k) = m(e_i)m(f_j) \quad (19)$$

Based on the original stress constraint $\sigma_{PN,k} < \sigma_{cons}$, the structural stress failure domain can be denoted as

$$\kappa = \{\sigma_{PN} | g(c_k, \sigma_{PN,k}) = \sigma_{cons} - \sigma_{PN,k} < 0, c_k \in C\} \quad (20)$$

Then the belief function $\text{Bel}(\kappa)$ and plausibility function $\text{Pl}(\kappa)$ of structural failure can be solved by Eq. (17). The focal element that has an intersection with the failure domain will be counted into $\text{Pl}(\kappa)$ as shown in Fig 3.

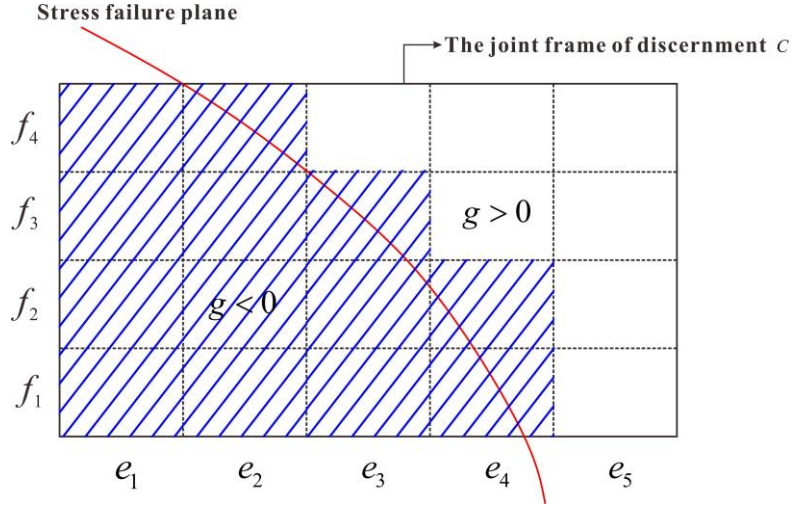


Fig 3 Stress failure domain of the joint FOD

Since $PI(\kappa)$ denotes the upper bound of structural failure probability, it is reasonable to constrain $PI(\kappa)$ as the stress failure probability:

$$PI\{g(C, \sigma_{PN}) < 0\} < P_f \quad (21)$$

where P_f denotes the value of stress failure probability constraint. Eventually, the original stress constraint $\sigma_{PN} < \sigma_{cons}$ is replaced by Eq. (21). The procedure of estimating the stress failure probability $PI(\kappa)$ is shown in Fig 4.

It can be predicted from the above descriptions that the accuracy and efficiency of the structural uncertainty analysis based on evidence theory mainly depend on the allocation of the focal elements. A fine focal element division can evaluate the structural failure probability more accurately but will decline the solving efficiency. Some discussions on evidence theory and other uncertainty analysis methods are as follows: (1) Compared with the non-probabilistic convex set method, evidence theory makes better use of the uncertain information, instead of only considering the parameter boundary. (2) Compared with the first-order reliability method, evidence theory works normally when the structural performance function is highly nonlinear, and can obtain higher accuracy by adjusting the focal element allocations, but may be inferior to FORM in terms of efficiency. (3) Compared with the Monte Carlo method, evidence theory can improve the accuracy by arranging the focal element meticulously, but it will also produce huge computational consumption, thus the accuracy and efficiency of both are related to the problem studied. Besides, the analysis process of evidence theory does not depend on the form of data source and does not need to consider the construction of random numbers as Monte Carlo simulation.

In fact, the greatest advantage of the evidence theory method compared with other

uncertainty analysis methods is its ability in fusing multi-source uncertainty parameters. In engineering practice, the common conditions are that the obtained data cannot accurately estimate the probability distribution of parameters, but the information is not just limited to the boundary of parameters. In this case, evidence theory can handle both random uncertainty and cognitive uncertainty data sources by data fusion. Compared with the traditional uncertainty analysis methods, evidence theory has the potential to assess reliability more accurately by fusing multi-source data.

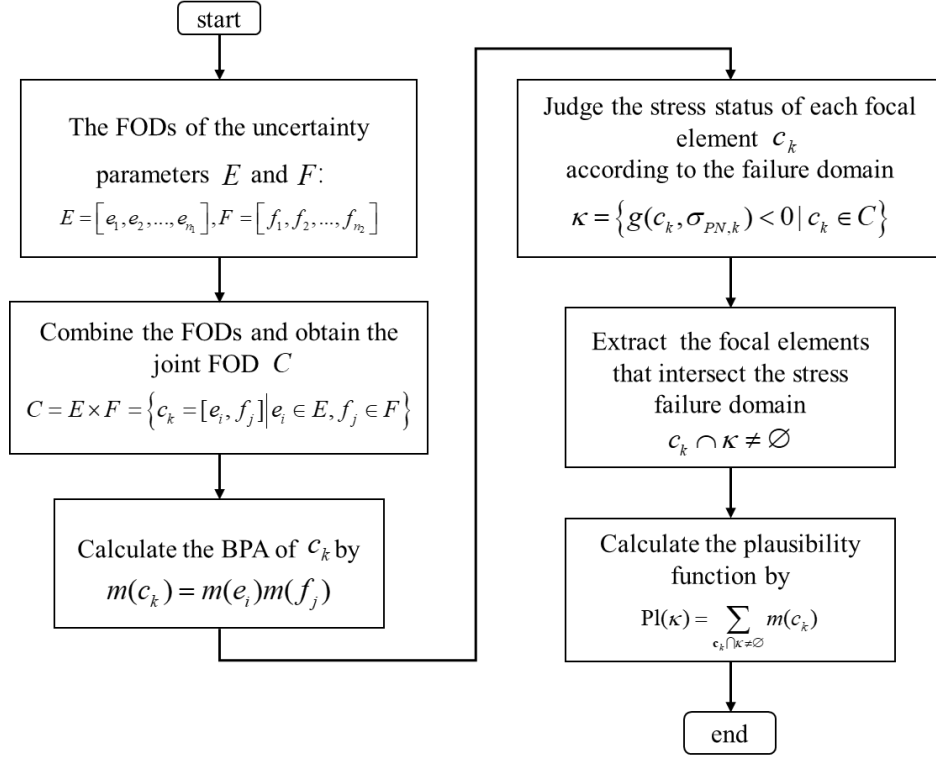


Fig 4 Estimation procedure of stress failure probability based on evidence theory

4 Framework of stress-constrained cross-scale reliability topology optimization based on evidence theory

In the previous chapter, the evidence theory is introduced to process the uncertainty parameters, the original global stress constraint is replaced by the failure probability to measure the stress failure. The optimal formulation can be rewritten as

$$\left. \begin{aligned}
 & \text{Double-scale formulation:} \\
 & \min_{\rho_i, P_j} : \bar{V} = \frac{\sum_{i=1}^N P_i \cdot V_i \cdot \frac{\sum_{j=1}^n \rho_j}{n}}{V}, \\
 & \quad i = 1, 2, 3, \dots, N, j = 1, 2, 3, \dots, n \\
 & \text{s.t.:} \\
 & \left. \begin{aligned}
 & \mathbf{K}(\mathbf{D}_{Mac}) \cdot \mathbf{U} = \mathbf{F}, \mathbf{D}_{Mac,i} = P_i^\alpha \cdot \mathbf{D}_H \\
 & \text{Pl}\{g(C, \sigma_{PN}) < 0\} < P_f \\
 & 0 < \delta \leq P_i \leq 1
 \end{aligned} \right\} \text{Macro} \\
 & \left. \begin{aligned}
 & \mathbf{K}(\mathbf{D}_0) \cdot \mathbf{U} = \mathbf{F}, \mathbf{D}_{Mic,j} = \rho_j^\alpha \cdot \mathbf{D}_0 \\
 & 0 < \delta \leq \rho_j \leq 1
 \end{aligned} \right\} \text{Micro}
 \end{aligned} \right\} \quad (22)$$

The optimal formulation and the sensitivity will differ from the deterministic optimization when considering uncertainty factors. This chapter will discuss the sensitivities and some details involved in optimization, including smoothing of the failure probability plausibility function, length scale control on cell microstructure, and sensitivity derivation of the constraint functions.

4.1 Smoothing of the failure probability plausibility function

In evidence theory, the framework of discernment of each uncertainty parameter constitutes the joint framework of discernment, and each focal element represents a sub-interval combination of the uncertainty parameter intervals. The structural response is solved under each focal element, and then the failure domain is used to determine the response failure probability of the whole structure.

Now consider the stress failure probability constraint defined by Eq. (21). If the upper bound of stress response $\sigma_{PN,k}$ under focal element c_k satisfies $\bar{\sigma}_{PN,k} > \sigma_{cons}$, then it is equal to $c_k \cap \kappa \neq \emptyset$. Therefore, Eq. (21) can be rewritten as

$$\text{Pl}(\kappa) = \sum_{k=1}^M m(c_k) \cdot I_{\sigma_{PN,k} > \sigma_{cons}}(\bar{\sigma}_{PN,k}) \leq P_f \quad (23)$$

where M is the number of focal elements, $I_{\sigma_{PN,k} > \sigma_{cons}}(\bar{\sigma}_{PN,k})$ is an indicator function:

$$I_{\sigma_{PN,k} > \sigma_{cons}}(\bar{\sigma}_{PN,k}) = \begin{cases} 1, & \bar{\sigma}_{PN,k} > \sigma_{cons} \\ 0, & \bar{\sigma}_{PN,k} \leq \sigma_{cons} \end{cases} \quad (24)$$

The indicator function will calculate the basic probability assignment of the focal element that

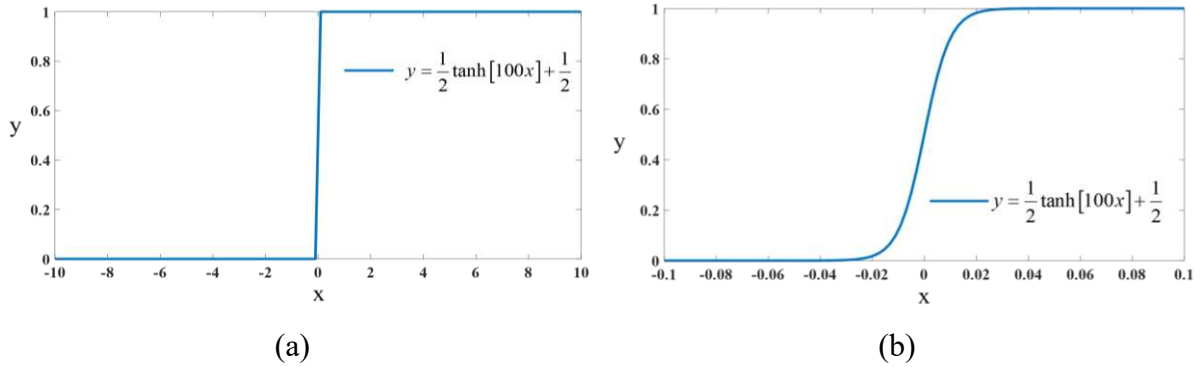
meets the failure condition $\bar{\sigma}_{PN,k} > \sigma_{cons}$ into $Pl(\kappa)$. Since the indicator function is discontinuous, the sensitivity required by the gradient algorithm for variable updating can't be solved. Note that the indicator function is a step function, it can be smoothed by a hyperbolic tangent function:

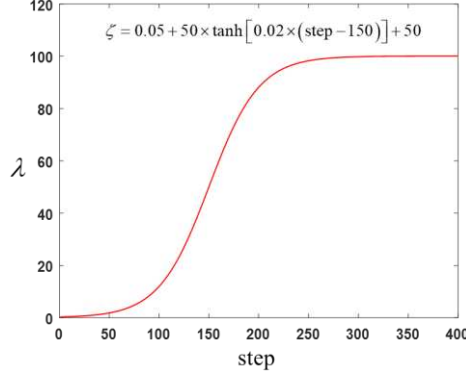
$$Pl(\kappa) = \sum_{k=1}^M m(c_k) \cdot I_{\bar{\sigma}_{PN,k} > \sigma_{cons}}(\bar{\sigma}_{PN,k}) \approx \sum_{k=1}^M m(c_k) \cdot \left\{ \frac{1}{2} \tanh \left[\zeta (\bar{\sigma}_{PN,k} - \sigma_{cons}) \right] + \frac{1}{2} \right\} \quad (25)$$

where the parameter ζ controls the degree of approximation, and the approximation effect will become better as ζ increases. To illustrate the effect of the approximation more clearly, plot the image of the hyperbolic tangent function $y(x) = \frac{1}{2} \tanh[100x] + \frac{1}{2}$ on $x \in [-10, 10]$ and $x \in [-0.1, 0.1]$ as shown in Fig 5(a) and Fig 5(b). Intuitively, the figure on $[-10, 10]$ is close to a step function. Take a tighter range of the argument ($x \in [-0.1, 0.1]$) and it can be observed that the image changes more drastically in the interval $[-0.03, 0.03]$ while the function is very close to a step function beyond $[-0.03, 0.03]$. It can be seen that the function can achieve a satisfying approximation effect when the interval between $\bar{\sigma}_{PN,k}$ and σ_{cons} is greater than 0.03, and it can also achieve a considerable effect within $[-0.03, 0.03]$. To reduce oscillation at the beginning of the iteration, ζ is also defined as a hyperbolic tangent function of the iteration steps:

$$\zeta = 0.05 + 50 \times \tanh \left[0.02 \times (\text{step} - 150) \right] + 50 \quad (26)$$

The curve of $\zeta - \text{step}$ is shown in Fig 5(c).





(c)

Fig 5 Partial curves of the hyperbolic tangent functions

4.2 The final optimization formulation based on the length scale control method

Small features that are not conducive to engineering often appear in the cell microstructure obtained by topology optimization, such as thin rods, small holes, hinges, etc. The actual stiffness and strength of these features often fail to meet the theoretical expectations. Therefore, it is often necessary to constrain the minimum length scale of the cell microstructure in the optimization process.

One of the main methods of applying length scale control is the density projection method based on the Heaviside function. This method processes the filtered density design variables by a projection threshold to obtain design results that meet the length scale constraint: The micro design variable ρ_j is first filtered by a certain filtering radius R_f :

$$\rho_j = \frac{\sum_{m \in O_{e,j}} \omega(\boldsymbol{\varsigma}_m) v_m \rho_m}{\sum_{m \in O_{e,j}} \omega(\boldsymbol{\varsigma}_m) v_m} \quad (27)$$

where $O_{e,j}$ is the neighborhood set of elements lying within the filter domain for element j , v_m denotes the volume of the element m in $O_{e,j}$, $\omega(\boldsymbol{\varsigma}_m)$ is the weighting function which is defined as

$$\omega(\boldsymbol{\varsigma}_m) = R_f - |\boldsymbol{\varsigma}_m - \boldsymbol{\varsigma}_j| \quad (28)$$

where $\boldsymbol{\varsigma}_m$ and $\boldsymbol{\varsigma}_j$ denote the central coordinates of the design cell j and m respectively, R_f is the filter radius which is specified. It is worth mentioning that density filtering and sensitivity filtering are common methods in preventing the ‘checkerboard effect’ phenomenon in density-based topology optimization (including multi-scale cases). In this paper, sensitivity filtering is conducted at the macro level to avoid computational complexity, and density filtering is conducted at the micro level to facilitate the implementation of the length scale control

method based on density projection.

The filtered density ρ_j is then projected to a new distribution, defined as the projected density [56]:

$$\bar{\rho}_j = \frac{\tanh(\beta\eta) + \tanh(\beta(\rho_j - \eta))}{\tanh(\beta\eta) + \tanh(\beta(1 - \eta))} \quad (29)$$

where β and η are parameters that control the effect of the projection. The final effect of the projection can be expressed by the Heaviside function:

$$\bar{\rho}_j = H(\rho_j, \eta) = \begin{cases} 0 & 0 \leq \rho_j < \eta \\ \eta & \rho_j = \eta \\ 1 & \eta < \rho_j \leq 1 \end{cases} \quad (30)$$

It is obvious that the role of the parameter η is to provide a projection threshold: After projection, all filtered density variables ρ_j above the threshold η will be projected to 1 and those below η will be projected to 0. The parameter β controls the approximation degree of the projection function to the Heaviside function: The larger β is, the closer the projected density is to the step distribution. There is a correspondence between η and minimum length scale b , so a cell microstructure with a specific minimum size can be obtained by selecting η reasonably.

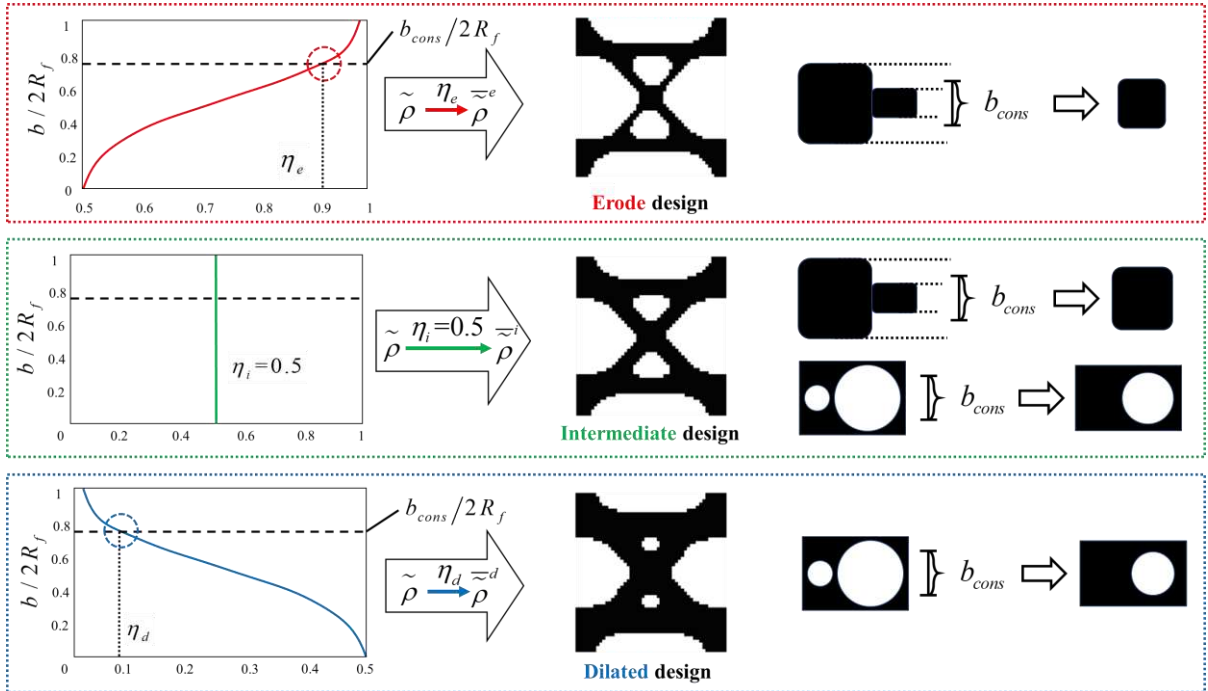


Fig 6 Length scale control effect of three density projection designs

Due to the need of controlling the length scale of the thin rod and the holes simultaneously, three different values of η are selected as η_e , η_i and η_d . The effect of three different η in minimum length scale control has been shown in Fig 6. The design result obtained by η_e is defined as the eroded design, which will eliminate the rods that are smaller than the length scale constraint. The design result obtained by η_d is defined as the dilated design, which will eliminate the holes that violate the length scale constraint. η_i takes a fixed value of 0.5, and the design result is defined as the intermediate design. The length scale of the microstructure in the intermediate design lays between the eroded design and the dilated design, so when all three designs reach stable convergence, the minimum length scale of the intermediate design will be controlled.

Add the length scale control method based on the density projection to the optimization model, the minimum length scale will be controlled by a recessive constraint. In addition, the stress is less sensitive to the changes of material stiffness properties than the changes of load while the changes of cell microstructures mainly affect the stiffness properties. Therefore, a displacement constraint is added to the optimization model to assist the formation of the cell microstructure. Finally, the optimization formulation can be expressed as

$$\begin{aligned}
 & \text{Double-scale formulation:} \\
 & \min_{\rho_i, P_j} : \bar{V}^d = \frac{\sum_{i=1}^N P_i \cdot V_i \cdot \frac{\sum_{j=1}^n \rho_j^{-d}(\rho)}{n}}{V}, \\
 & \quad i = 1, 2, 3, \dots, N, j = 1, 2, 3, \dots, n \\
 & \text{s.t.:} \\
 & \left. \begin{aligned}
 & \mathbf{K}(\mathbf{D}_{mac}) \cdot \mathbf{U} = \mathbf{F}, \mathbf{D}_{mac,i} = P_i^\alpha \cdot \mathbf{D}_H \\
 & \text{Pl}\{g^i(\mathbf{C}, \sigma_{PN}) < 0\} < P_f \\
 & u_k^e \leq u_{cons,k}, k = 1, 2, \dots, M \\
 & 0 < \delta \leq P_i \leq 1
 \end{aligned} \right\} \text{Macro} \\
 & \left. \begin{aligned}
 & \mathbf{K}(\mathbf{D}_0) \cdot \mathbf{U} = \mathbf{F}, \mathbf{D}_{Mic,j} = \rho_j^\alpha \cdot \mathbf{D}_0 \\
 & \bar{v}^d = \frac{\sum_{j=1}^n \rho_j^{-d}(\rho)}{n} \leq v_{cons}^d \\
 & b \geq b_{cons} \\
 & 0 < \delta \leq \rho_j \leq 1
 \end{aligned} \right\} \text{Micro}
 \end{aligned} \tag{31}$$

where u_k is the displacement of the k -th constraint point, $u_{cons,k}$ is the k -th displacement

constraint, b is the minimum length scale of the cell microstructure, superscript e stands for the eroded design, superscript i stands for the intermediate design, superscript d stands for the dilated design. PI represents the structural stress response failure probability under evidence theory, thus the relationship between PI and structural reliability indicator R can be defined as

$$PI=1-R \quad (32)$$

Similarly, structural target reliability $R_{t, \text{arg}}$ is defined as $R_{t, \text{arg}}=1-P_f$.

4.3 Sensitivity analysis

The design variables are updated by the MMA algorithm, which updates the design variables by the gradient information. The sensitivity of the constraint function with respect to the design variables will be derived in this section.

The sensitivity of the plausibility function $PI(\kappa)$ with respect to the macro design variable and the micro design variable can be depicted as

$$\begin{aligned} \frac{\partial PI(\kappa)}{\partial P_i} &= \frac{\partial \sum_{k=1}^M m(c_k) \cdot \left\{ \frac{1}{2} \tanh \left[\zeta \left(\bar{\sigma}_{PN,k} - \sigma_{cons} \right) \right] + \frac{1}{2} \right\}}{\partial P_i} \\ &= \sum_{k=1}^M \frac{\partial m(c_k) \cdot \left\{ \frac{1}{2} \tanh \left[\zeta \left(\bar{\sigma}_{PN,k} - \sigma_{cons} \right) \right] + \frac{1}{2} \right\}}{\partial P_i} \\ \frac{\partial PI(\kappa)}{\partial \rho_j} &= \frac{\partial \sum_{k=1}^M m(c_k) \cdot \left\{ \frac{1}{2} \tanh \left[\zeta \left(\bar{\sigma}_{PN,k} - \sigma_{cons} \right) \right] + \frac{1}{2} \right\}}{\partial \rho_j} \\ &= \sum_{k=1}^M \frac{\partial m(c_k) \cdot \left\{ \frac{1}{2} \tanh \left[\zeta \left(\bar{\sigma}_{PN,k} - \sigma_{cons} \right) \right] + \frac{1}{2} \right\}}{\partial \rho_j} \end{aligned} \quad (33)$$

which can be rewritten utilizing the chain derivation rule as

$$\begin{aligned}
 \frac{\partial \text{Pl}(\kappa)}{\partial P_i} &= \sum_{k=1}^M \frac{\partial pl_k(\kappa)}{\partial \bar{\sigma}_{PN,k}} \cdot \frac{\partial \bar{\sigma}_{PN,k}}{\partial P_i} \\
 &= \sum_{k=1}^M \frac{\partial m(c_k) \cdot \left\{ \frac{1}{2} \tanh \left[\zeta \left(\bar{\sigma}_{PN,k} - \sigma_{cons} \right) \right] + \frac{1}{2} \right\}}{\partial \bar{\sigma}_{PN,k}} \cdot \frac{\partial \bar{\sigma}_{PN,k}}{\partial P_i} \\
 \frac{\partial \text{Pl}(\kappa)}{\partial \rho_j} &= \sum_{k=1}^M \frac{\partial pl_k(\kappa)}{\partial \bar{\sigma}_{PN,k}} \cdot \frac{\partial \bar{\sigma}_{PN,k}}{\partial \rho_j} \\
 &= \sum_{k=1}^M \frac{\partial m(c_k) \cdot \left\{ \frac{1}{2} \tanh \left[\zeta \left(\bar{\sigma}_{PN,k} - \sigma_{cons} \right) \right] + \frac{1}{2} \right\}}{\partial \bar{\sigma}_{PN,k}} \cdot \frac{\partial \bar{\sigma}_{PN,k}}{\partial \rho_j}
 \end{aligned} \tag{34}$$

where the derivative $\frac{\partial pl_k(\kappa)}{\partial \bar{\sigma}_{PN,k}}$ can be easily calculated:

$$\begin{aligned}
 \frac{\partial pl_k(\kappa)}{\partial \bar{\sigma}_{PN,k}} &= \frac{\partial \sum_{k=1}^M m(c_k) \cdot \left\{ \frac{1}{2} \tanh \left[\zeta \left(\bar{\sigma}_{PN,k} - \sigma_{cons} \right) \right] + \frac{1}{2} \right\}}{\partial \bar{\sigma}_{PN,k}} \\
 &= \frac{1}{2} m(c_k) \cdot \zeta \cdot \left\{ 1 - \tanh^2 \left[\zeta \left(\bar{\sigma}_{PN,k} - \sigma_{cons} \right) \right] \right\}
 \end{aligned} \tag{35}$$

Therefore, the main task is to solve the derivative of $\bar{\sigma}_{PN,k}$ with respect to the design variables: $\frac{\partial \bar{\sigma}_{PN,k}}{\partial P_i}$ and $\frac{\partial \bar{\sigma}_{PN,k}}{\partial \rho_j}$. Considering that the uncertainty parameters E and P are independent variables, the upper and lower bounds of the structural stress response corresponding to each focal element c_k are located at the apex of the hypercube. In order to simplify the explanation, the solution of the stress sensitivity derivation $\frac{\partial \sigma_{PN}}{\partial P_i}$ and $\frac{\partial \sigma_{PN}}{\partial \rho_j}$ will be illustrated instead of $\frac{\partial \bar{\sigma}_{PN,k}}{\partial P_i}$ and $\frac{\partial \bar{\sigma}_{PN,k}}{\partial \rho_j}$.

(1) The sensitivity of σ_{PN} with respect to the macro density design variables:

$$\begin{aligned}
 \frac{\partial \sigma_{PN}}{\partial P_i} &= \frac{\partial \left[c \cdot \left(\sum_{k=1}^N \sigma_{vM,k}^q \right)^{\frac{1}{q}} \right]}{\partial P_i} \\
 &= \frac{c}{q} \cdot \left(\sum_{k=1}^N \sigma_{vM,k}^q \right)^{\frac{1}{q}-1} \cdot q \cdot \sum_{k=1}^N \left(\sigma_{vM,k}^{q-1} \cdot \frac{\partial \sigma_{vM,k}}{\partial \sigma_k^T} \cdot \frac{\partial \sigma_k}{\partial P_i} \right)
 \end{aligned} \tag{36}$$

The stress matrix $\boldsymbol{\sigma}_k$ of the k -th macro element is

$$\boldsymbol{\sigma}_k = P_k^s \mathbf{D}_H \mathbf{B} \mathbf{u}_k^e \quad (37)$$

where \mathbf{B} is the FE strain-displacement gradient matrix, \mathbf{u}_k^e is the nodal displacement vector of the k -th macro element, s is the stress penalty factor. Substitute Eq. (37) into Eq. (36) gives

$$\frac{\partial \sigma_{PN}}{\partial P_i} = \bar{C} \cdot \sigma_{vM,i}^{q-1} \cdot \frac{\partial \sigma_{vM,k}}{\partial \boldsymbol{\sigma}_k^T} \cdot s \cdot P_i^{s-1} \mathbf{D}_H \mathbf{B} \mathbf{u}_i^e + \bar{C} \cdot \sum_{k=1}^N \left[\sigma_{vM,k}^{q-1} \cdot \frac{\partial \sigma_{vM,k}}{\partial \boldsymbol{\sigma}_k^T} \cdot P_k^s \mathbf{D}_H \mathbf{B} \frac{\partial \mathbf{u}_k^e}{\partial P_i} \right] \quad (38)$$

where $\bar{C} = c \left(\sum_{k=1}^N \sigma_{vM,k}^q \right)^{\frac{1}{q}-1}$. Since the second part of Eq. (38) contains all the macro elements, it can be simplified as

$$\bar{C} \cdot \sum_{k=1}^N \left[\sigma_{vM,k}^{q-1} \cdot \frac{\partial \sigma_{vM,k}}{\partial \boldsymbol{\sigma}_k^T} \cdot P_k^s \mathbf{D}_H \mathbf{B} \frac{\partial \mathbf{u}_k^e}{\partial P_i} \right] = \sum_{r=1}^{N_f} \left(h_r \cdot \frac{\partial u_r}{\partial P_i} \right) \quad (39)$$

where N_f denotes the dimension of the global displacement \mathbf{u} , u_r is the r -th element of \mathbf{u} , h_r can be calculated using Eq. (39).

$\frac{\partial u_r}{\partial P_i}$ can be solved by the adjoint method by introducing the Lagrange multiplier:

$$u_r = u_r + \boldsymbol{\lambda}_r^T (\mathbf{F} - \mathbf{K} \mathbf{u}) \quad (40)$$

Since the FE equilibrium equation $\mathbf{K} \mathbf{u} = \mathbf{F}$ is satisfied, Eq. (40) is equal to $u_r \equiv u_r$. Therefore,

$\frac{\partial u_r}{\partial P_i}$ can be depicted as

$$\frac{\partial u_r}{\partial P_i} = \left(\frac{\partial u_r}{\partial \mathbf{u}} - \boldsymbol{\lambda}_r^T \mathbf{K} \right) \frac{d\mathbf{u}}{dP_i} + \boldsymbol{\lambda}_r^T \left(\frac{d\mathbf{F}}{dP_i} - \frac{\partial \mathbf{K}}{\partial P_i} \mathbf{u} \right) \quad (41)$$

Since Eq.(41) holds for any $\boldsymbol{\lambda}_r^T$, the coefficient of $\frac{d\mathbf{u}}{dP_i}$ will be zero when $\boldsymbol{\lambda}_r^T$ satisfies

$$\frac{\partial u_r}{\partial \mathbf{u}} - \boldsymbol{\lambda}_r^T \mathbf{K} = 0 \quad (42)$$

Utilizing symmetry, Eq.(42) can be rewritten as

$$\mathbf{K} \boldsymbol{\lambda}_r = \left(\frac{\partial u_r}{\partial \mathbf{u}} \right)^T \quad (43)$$

Consequently, regarding $\left(\frac{\partial u_r}{\partial \mathbf{u}}\right)^T$ as a load, the Lagrange multiplier λ_r can be solved by FEA.

Since the external load is independent of the density variables, derivation $\frac{\partial u_r}{\partial P_i}$ can be depicted

as

$$\frac{\partial u_r}{\partial P_i} = -\lambda_r^T \frac{\partial \mathbf{K}}{\partial P_i} \mathbf{u} \quad (44)$$

Therefore, the second term of Eq. (38) can be rewritten as

$$\bar{C} \cdot \sum_{k=1}^N \left[\sigma_{vM,k}^{q-1} \cdot \frac{\partial \sigma_{vM,k}}{\partial \boldsymbol{\sigma}_k^T} \cdot P_k^s \mathbf{D}_H \mathbf{B} \frac{\partial \mathbf{u}_k^e}{\partial P_i} \right] = - \sum_{r=1}^{N_f} \left(h_r \lambda_r^T \frac{\partial \mathbf{K}}{\partial P_i} \mathbf{u} \right) = - \left(\sum_{r=1}^{N_f} h_r \lambda_r^T \right) \cdot \frac{\partial \mathbf{K}}{\partial P_i} \mathbf{u} \quad (45)$$

Since the displacement of the linear elastic structure can be superimposed, $\sum_{r=1}^{N_f} h_r \lambda_r^T$ can be

solved in one finite element analysis: Impose a virtual load column vector $\sum_{r=1}^{N_f} \left[h_r \left(\frac{\partial u_r}{\partial \mathbf{u}} \right)^T \right]$ on

the whole structure and the displacement response vector is $\sum_{r=1}^{N_f} h_r \lambda_r^T$. Substituting Eq.(45) into

Eq.(38), the final expression of $\frac{\partial \sigma_{PN}}{\partial P_i}$ is

$$\frac{\partial \sigma_{PN}}{\partial P_i} = \bar{C} \cdot \sigma_{vM,i}^{q-1} \cdot \frac{\partial \sigma_{vM,i}}{\partial \boldsymbol{\sigma}_i^T} \cdot s \cdot P_i^{s-1} \mathbf{D}_H \mathbf{B} \mathbf{u}_i^e - \left(\sum_{r=1}^{N_f} h_r \lambda_r^T \right) \frac{\partial \mathbf{K}}{\partial P_i} \mathbf{u} \quad (46)$$

(2) The sensitivity of σ_{PN} with respect to the micro density design variables ρ_j :

$$\frac{\partial \sigma_{PN}}{\partial \rho_j} = \frac{\partial \left[c \cdot \left(\sum_{k=1}^N \sigma_{vM,k}^q \right)^{\frac{1}{q}} \right]}{\partial \rho_j} = \frac{c}{q} \cdot \left(\sum_{k=1}^N \sigma_{vM,k}^q \right)^{\frac{1}{q}-1} \cdot q \cdot \sum_{k=1}^N \left(\sigma_{vM,k}^{q-1} \cdot \frac{\partial \sigma_{vM,k}}{\partial \boldsymbol{\sigma}_k^T} \cdot \frac{\partial \boldsymbol{\sigma}_k}{\partial \rho_j} \right) \quad (47)$$

Substitute the expression of $\boldsymbol{\sigma}_k$, yields

$$\begin{aligned}
 \frac{\partial \sigma_{PN}}{\partial \rho_j} &= \frac{c}{q} \cdot \left(\sum_{k=1}^N \sigma_{vM,k}^q \right)^{\frac{1}{q}-1} \cdot q \cdot \sum_{k=1}^N \left[\sigma_{vM,k}^{q-1} \cdot \frac{\partial \sigma_{vM,k}}{\partial \boldsymbol{\sigma}_k^T} \cdot \left(P_k^s \frac{\partial \mathbf{D}_H}{\partial \rho_j} \mathbf{B} \mathbf{u}_k^e + P_k^s \mathbf{D}_H \mathbf{B} \frac{\partial \mathbf{u}_k^e}{\partial \rho_j} \right) \right] \\
 &= \bar{C} \cdot \sum_{k=1}^N \left[\sigma_{vM,k}^{q-1} \cdot \frac{\partial \sigma_{vM,k}}{\partial \boldsymbol{\sigma}_k^T} \cdot \left(P_k^s \frac{\partial \mathbf{D}_H}{\partial \rho_j} \mathbf{B} \mathbf{u}_k^e + P_k^s \mathbf{D}_H \mathbf{B} \frac{\partial \mathbf{u}_k^e}{\partial \rho_j} \right) \right] \\
 &= \bar{C} \cdot \sum_{k=1}^N \left[\sigma_{vM,k}^{q-1} \cdot \frac{\partial \sigma_{vM,k}}{\partial \boldsymbol{\sigma}_k^T} \cdot P_k^s \frac{\partial \mathbf{D}_H}{\partial \rho_j} \mathbf{B} \mathbf{u}_k^e \right] + \bar{C} \cdot \sum_{k=1}^N \left[\sigma_{vM,k}^{q-1} \cdot \frac{\partial \sigma_{vM,k}}{\partial \boldsymbol{\sigma}_k^T} \cdot P_k^s \mathbf{D}_H \mathbf{B} \frac{\partial \mathbf{u}_k^e}{\partial \rho_j} \right]
 \end{aligned} \tag{48}$$

where $\bar{C} = c \left(\sum_{k=1}^N \sigma_{vM,k}^q \right)^{\frac{1}{q}-1}$. The second term of Eq.(48) can be simplified by the same method

used in the solution of the macro sensitivity:

$$\bar{C} \cdot \sum_{k=1}^N \left[\sigma_{vM,k}^{q-1} \cdot \frac{\partial \sigma_{vM,k}}{\partial \boldsymbol{\sigma}_k^T} \cdot P_k^s \mathbf{D}_H \mathbf{B} \frac{\partial \mathbf{u}_k^e}{\partial \rho_j} \right] = - \sum_{r=1}^{N_f} \left(h_r \boldsymbol{\lambda}_r^T \frac{\partial \mathbf{K}}{\partial \rho_j} \mathbf{u} \right) = - \left(\sum_{r=1}^{N_f} h_r \boldsymbol{\lambda}_r^T \right) \frac{\partial \mathbf{K}}{\partial \rho_j} \mathbf{u} \tag{49}$$

where $\sum_{r=1}^{N_f} h_r \boldsymbol{\lambda}_r^T$ can also be obtained by imposing a virtual load column vector $\sum_{r=1}^{N_f} \left[h_r \left(\frac{\partial \mathbf{u}_r}{\partial \mathbf{u}} \right)^T \right]$,

$\frac{\partial \mathbf{K}}{\partial \rho_j}$ can be expanded as

$$\frac{\partial \mathbf{K}}{\partial \rho_j} = \frac{\partial \left(\sum_{i=1}^n P_i^\alpha \int_{\Omega_i} \mathbf{B}^T \mathbf{D}_H \mathbf{B} d\Omega \right)}{\partial \rho_j} = \sum_{i=1}^n P_i^\alpha \int_{\Omega_i} \mathbf{B}^T \frac{\partial \mathbf{D}_H}{\partial \rho_j} \mathbf{B} d\Omega \tag{50}$$

where $\frac{\partial \mathbf{D}_H}{\partial \rho_j}$ can be calculated by a projection method [57]:

$$\frac{\partial \mathbf{D}_H}{\partial \rho_j} = \alpha \rho_j^{\alpha-1} \int_{Y_j} (\mathbf{I} - \mathbf{b} \mathbf{u}_j)^T \mathbf{D}_0 (\mathbf{I} - \mathbf{b} \mathbf{u}_j) dY \tag{51}$$

where \mathbf{I} is an identity diagonal matrix, \mathbf{b} is the strain matrix of the elements in the micro design domain, \mathbf{u}_j is the displacement matrix of the j -th microelement, \mathbf{D}_0 is the elastic matrix of the material, Y_j is the j -th microelement domain. Substituting Eq.(49), Eq.(50),

and Eq.(51), into Eq.(48), the final expression of $\frac{\partial \sigma_{PN}}{\partial \rho_j}$ is

$$\begin{aligned} \frac{\partial \sigma_{PN}}{\partial \rho_j} = & \bar{C} \cdot \sum_{k=1}^N \left[\sigma_{vM,k}^{q-1} \cdot \frac{\partial \sigma_{vM,k}}{\partial \boldsymbol{\sigma}_k^T} \cdot P_k^s \frac{\partial \mathbf{D}_H}{\partial \rho_j} \mathbf{B} \mathbf{u}_k^e \right] \\ & - \left(\sum_{r=1}^{N_f} h_r \boldsymbol{\lambda}_r^T \right) \cdot \sum_{i=1}^N \left[\alpha \rho_j^{\alpha-1} P_i^\alpha \int_{\Omega_i} \mathbf{B}^T \left(\int_{Y_j} (\mathbf{I} - \mathbf{b} \mathbf{u}_j)^T \mathbf{D}_0 (\mathbf{I} - \mathbf{b} \mathbf{u}_j) dY \right) \mathbf{B} d\Omega \right] \cdot \mathbf{u} \end{aligned} \quad (52)$$

Since the micro design variable ρ has been filtered and projected to realize micro length scale control, the sensitivity of $\text{Pl}(\kappa)$ with respect to ρ_j should be

$$\begin{aligned} \frac{\partial \text{Pl}(\kappa)}{\partial \rho_j} &= \sum_{i \in \mathbb{N}_{e,j}} \frac{\partial \text{Pl}(\kappa)}{\partial \rho_i} \cdot \frac{\partial \bar{\rho}_i}{\partial \rho_i} \cdot \frac{\partial \rho_i}{\partial \rho_j} \\ &= \sum_{i \in \mathbb{N}_{e,j}} \left(\sum_{k=1}^M \frac{\partial p_l(\kappa)}{\partial \sigma_{PN,k}} \cdot \frac{\partial \bar{\sigma}_{PN,k}}{\partial \rho_i} \right) \cdot \frac{\partial \bar{\rho}_i}{\partial \rho_i} \cdot \frac{\partial \rho_i}{\partial \rho_j} \end{aligned} \quad (53)$$

where the expressions of $\frac{\partial \bar{\rho}_i}{\partial \rho_i}$ and $\frac{\partial \rho_i}{\partial \rho_j}$ are

$$\begin{aligned} \frac{\partial \bar{\rho}_i}{\partial \rho_i} &= \frac{\beta \cdot \text{sech}^2(\beta(\rho_i - \eta))}{\tanh(\beta\eta) + \tanh(\beta(1-\eta))} \\ \frac{\partial \rho_i}{\partial \rho_j} &= \frac{w(\boldsymbol{\zeta}_j) v_j}{\sum_{m \in \mathbb{N}_{e,i}} w(\boldsymbol{\zeta}_m) v_m} \end{aligned} \quad (54)$$

The sensitivities of other constraints are

$$\begin{aligned} \frac{\partial u_k}{\partial P_i} &= -\alpha P_i^{\alpha-1} \boldsymbol{\lambda}_{k,i}^T \mathbf{K}_{e0,i} \mathbf{u}_{e,i} \\ \frac{\partial u_k}{\partial \rho_j} &= \sum_{i \in \mathbb{N}_{e,j}} \left(-\boldsymbol{\lambda}_k^T \sum_{i=1}^n P_i^\alpha \int_{\Omega_i} \mathbf{B}^T \frac{\partial \mathbf{D}_H}{\partial \rho_i} \mathbf{B} d\Omega \cdot \mathbf{u} \right) \cdot \frac{\partial \bar{\rho}_i}{\partial \rho_i} \cdot \frac{\partial \rho_i}{\partial \rho_j} \end{aligned} \quad (55)$$

where $\mathbf{K}_{e0,i}$ is the stiffness matrix of the i -th macro element, $\mathbf{u}_{e,i}$ is the nodal displacement vector of the i -th macro element, $\boldsymbol{\lambda}_k^T$ can be solved by Eq.(43).

The macro and micro sensitivities of the objective function \bar{V} are

$$\begin{aligned}
 \frac{\partial \bar{V}}{\partial P_i} &= \frac{V_i \cdot \frac{\sum_{j=1}^n \bar{\rho}_j(\rho)}{n}}{\sum_{i=1}^N V_i} \\
 \frac{\partial \bar{V}}{\partial \rho_j} &= \sum_{i \in \mathbb{N}_{e,j}} \frac{\sum_{i=1}^N P_i \cdot V_i \cdot \frac{1}{n}}{\sum_{i=1}^N V_i} \cdot \frac{\partial \bar{\rho}_i}{\partial \rho_i} \cdot \frac{\partial \bar{\rho}_i}{\partial \rho_j} \\
 &= \sum_{i \in \mathbb{N}_{e,j}} \left(\frac{\sum_{i=1}^N P_i \cdot V_i \cdot \frac{1}{n}}{\sum_{i=1}^N V_i} \cdot \frac{\beta \cdot \text{sech}^2(\beta(\rho_i - \eta))}{\tanh(\beta\eta) + \tanh(\beta(1-\eta))} \cdot \frac{w(\xi_j)v_j}{\sum_{m \in \mathbb{N}_{e,i}} w(\xi_m)v_m} \right)
 \end{aligned} \tag{56}$$

where V_i is the volume of the i -th macro element.

5 Discussions on the optimization procedure and the computational scale

5.1 Procedure of the optimization

The entire optimization procedure of the proposed topology optimization is described as follows:

Step 1: Set the iteration step(h) to 1. Initiate the optimization parameters: macro density design variables $P_i|^{h}$, micro density design variables $\rho_j|^{h}$. Define the optimization parameters: density filtering radius R_f , failure probability constraint P_f , minimum length scale constraint b_{cons} , projection parameter β , the distribution of the uncertainty parameters E and F .

Step 2: Filter and project the micro density design variables. Determine the projection control parameter η_e , η_i and η_d based on the density filtering radius R_f and the minimum length scale constraint b_{cons} . Then process $\rho_j|^{h}$ by Eq. (27) and Eq. (29) with η_e , η_i and η_d to obtain $\bar{\rho}_j|^{h}$.

Step 3: Combine the intervals of the uncertainty parameters to obtain the joint framework of discernment C , extract the combination of vertices in each focal element c_k that maximizes the stress plausibility function:

$$\left\{ (\tilde{e}_k, f_k) \mid \sigma_{PN}(\tilde{e}_k, f_k) = \max[\sigma_{PN}(e_l, f_l)], (e_l, f_l, \tilde{e}_k, f_k) \in c_k \right\} \tag{57}$$

Then utilize the homogenization theory to solve the elastic modulus of the corresponding cell

microstructure.

Step 4: Utilize the vertices extracted in step 3 to solve the upper bound of σ_{pN} under each focal element c_k and impose the virtual load $\sum_{r=1}^{ndof} \left[h_r \left(\frac{\partial u_j}{\partial \mathbf{u}} \right)^T \right]$ to solve $\sum_{r=1}^{ndof} h_r \lambda_r^T$.

Step 5: Solve the structural failure plausibility $Pl(\kappa)$ using the structural response data obtained by the finite element analysis in step 4. Calculate the objective function and other constraint function values, and then calculate the macro and micro sensitivity by Eq.(46), Eq.(52), Eq.(55), and Eq.(56).

Step 6: Update the design variables by the MMA algorithm. Input the objective function, the constraint function, and the corresponding sensitivity to the MMA algorithm to update macro and micro density design variables (P_i^{h+1} and ρ_j^{h+1}).

Step 7: Use the convergence criterion to determine whether the iteration result meets the convergence condition:

$$\frac{\sum_{j=1}^n |\rho_j^{h+1} - \rho_j^h|}{n} < \varepsilon, \frac{\sum_{i=1}^N |P_i^{h+1} - P_i^h|}{N} < \varepsilon \quad (58)$$

where h denotes the step of the iteration. If the convergence criterion is satisfied, stop iterating and output the optimization result. If it is not satisfied, increase the number of iterations by one and return to step 2.

The schematic diagram of the optimization procedure is shown in Fig 7.

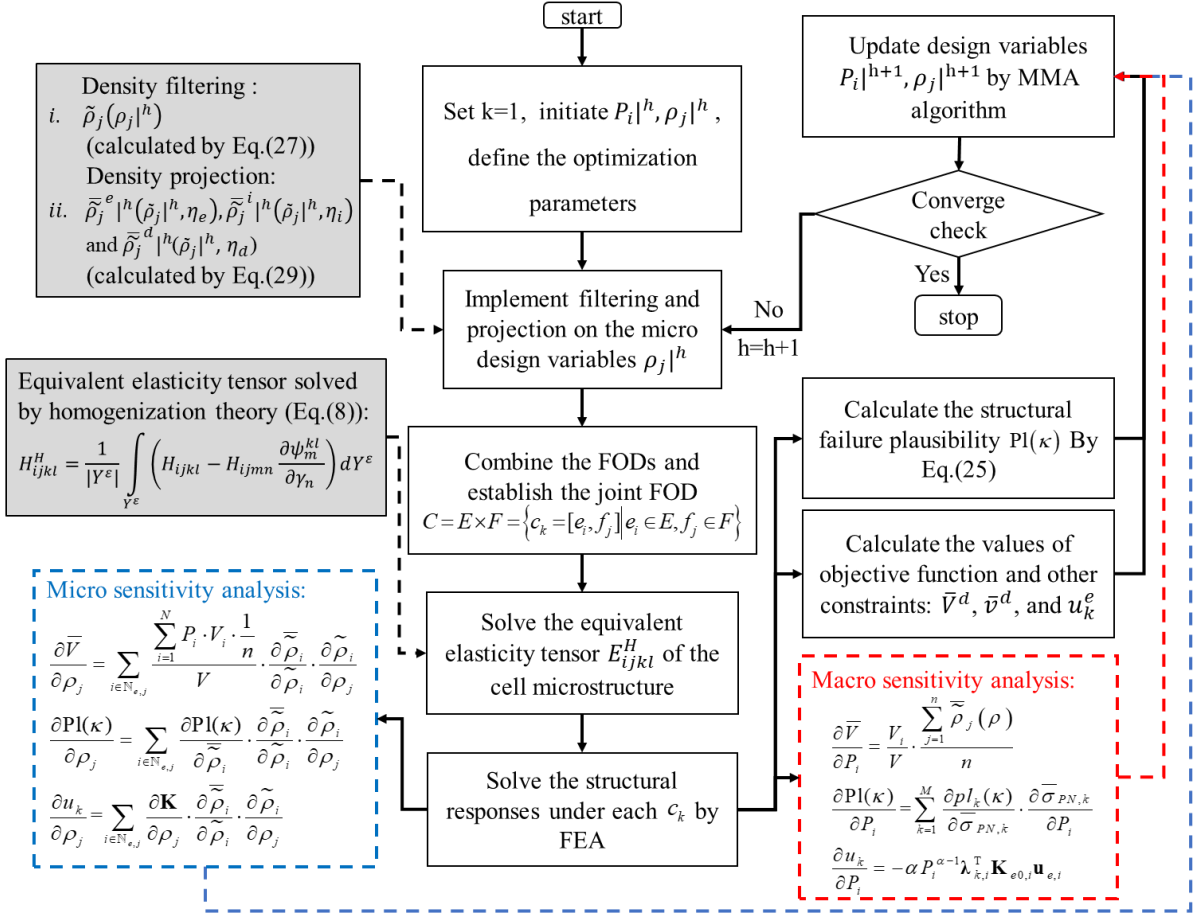


Fig 7 Procedure of optimization iteration

5.2 Discussions on the computational consumption

Compared with conventional stress-constrained topology optimization, cross-scale topology optimization introduces an extra design domain of the cell microstructure, which greatly increases the computational consumption. In this paper, the length scale control of the cell microstructure is introduced into the cross-scale optimization, and the uncertainty factors in the optimization parameters are considered. The optimization model in this paper involves two major computational consumption problems: The first one is the multiple calculations under different length scale control parameters η ; the second one is the introduction of evidence theory for structural reliability which requires finite element analysis under each focal element c_k .

The minimum length scale constraint in this paper is applied by projecting the micro design variables ρ_j , and the control effect is applied by selecting the projection parameter η . This method theoretically requires three finite element analyses at each iteration: the dilated design, the intermediate design, and the eroded design, so the computational consumption will be directly tripled. However, although the optimization process involves three different design

results, the structural volume fraction of the dilated design must be the largest of the three, so it only needs to consider the objective function of the dilated design. Therefore, the objective function and the cell volume fraction constraint can be simplified as

$$\bar{V}^d = \frac{\sum_{i=1}^N P_i \cdot V_i \cdot \frac{\sum_{j=1}^n \rho_j^{-d}(\rho)}{n}}{V} \quad (59)$$

$$\bar{v}_{Mic}^{-d} \leq v_{cons}^d$$

where the superscript d denotes the dilated design. Since the stiffness performance of the erode design is the lowest, the displacement constraint can be simplified as

$$u_k^e \leq u_{cons,k}, k = 1, 2, \dots, M \quad (60)$$

When the displacement constraint of the erode design is satisfied, the displacement constraint of the other two designs can also be satisfied. As for the stress constraint, considering the intermediate design will be selected as the final design result, the stress reliability constraint is only imposed on the intermediate design:

$$Pl\{g^i(C, \sigma_{PN}) < 0\} < P_f \quad (61)$$

It can be seen from the above analysis that it's not necessary to perform three series of finite element analysis in each step of the iteration. It only requires one series of finite element solutions respectively when solving the stress reliability constraint and the displacement constraint. Therefore, the computational consumption has not been greatly increased after introducing the length scale control.

In terms of the computational consumption of structural stress failure probability function based on evidence theory, considering that the components of the focal element are independent of each other and the structural response is monotonous with respect to the uncertainty parameters, the upper and lower bound of stress under each focal element can be solved using the vertex method. However, although the vertex method initially reduces the computational consumption, as the number of uncertainty parameters increases, the number of vertex combinations will also increase exponentially. Note that only the upper bound of $\sigma_{PN,k}$ is used in the expressions of $Pl(\kappa)$ and the sensitivity, the vertex method can be further simplified by extracting a combination that maximizes $\sigma_{PN,k}$. Such a combination of vertices is easy to obtain when the uncertainty parameters are monotonically related to the structural response. Therefore, when calculating the failure probability, one finite element analysis equivalent to the number

of focal elements of the joint identification frame is required, and most of the parameters required for sensitivity analysis can be obtained during this process. In addition, when solving the stress upper bound corresponding to each focal element, the external load vector needs to

be replaced by the virtual load $\sum_{r=1}^{ndof} \left[h_r \left(\frac{\partial u_j}{\partial \mathbf{u}} \right)^T \right]$ to solve $\sum_{r=1}^{ndof} h_r \lambda_r^T$ required by sensitivity analysis.

Table 1 The computational consumption in each stage of iteration

Object of solution	Number of FEA in each iteration
Density projection	$\bar{\rho}^{-e}, \rho^{-i}, \rho^{-d}$ (3 times) $\rightarrow \bar{\rho}^{-e}$ (1 time)
Plausibility $PI(\kappa)$	Each vertex of c_k (4 times) \rightarrow One vertex of c_k
Sensitivity of $PI(\kappa)$	One time under the virtual load $\sum_{r=1}^{ndof} \left[h_r \left(\frac{\partial u_j}{\partial \mathbf{u}} \right)^T \right]$
Displacement u_k	M times
Sensitivity of u_k	M times

In summary, in each iteration step, the number of the finite element analysis that needs to be conducted to solve the stress reliability constraint is twice the number of the focal element c_k . The number of FEA to solve the displacement constraint is twice the number of the displacement constraints in each iteration step. The number of FEA in each iteration is shown in Table 1. In addition, it is worth mentioning that the homogenization process of the microstructure will incur a large amount of computational consumption if the microstructures are macro-spatially varying. In this study, the computational consumption of homogenization is relatively small because of the assumption of macro-spatially uniform microstructures.

6 Numerical examples

In this chapter, three numerical examples are presented to illustrate the applicability of the proposed cross-scale topology optimization strategy. Due to the particularity of the micro sensitivity expressions, the values of the micro sensitivities will be the same under an average micro density distribution. Therefore, a preset initial cell material distribution is utilized in each example to provide a direction for the gradient algorithm. The computational environment of

the hardware is a computer with 16G RAM (Inter(R) Corel(TM) i7-8700K 3.70GHz), and it takes about 4 mins for one iteration step in the following examples.

6.1 Optimization of a cantilever beam

The macro design domain in this example is a rectangular cantilever beam fixed on the left side with a thickness of 1mm as shown in Fig 8. Two concentrated forces are imposed on the bottom left corner and the middle of the left side respectively. The micro design domain is an element of the macro design domain with the geometrical measure of 1mm×1mm and the thickness of 1mm. The optimization objective is minimizing the entire structural volume fraction. The macro and micro design domains are divided into 3200 and 1600 elements respectively by four-node plane elements. The uncertainty of the material Young's modulus and the external loads are considered. Assuming that there exists a normal distribution and another preset distribution for all the uncertainty parameters, which are synthesized by Eq.(13). The normal distribution parameters are defined as: $\mu_E = 70e3$ MPa , $\sigma_E = 4$, $\mu_{F_1} = 120N$, $\sigma_{F_1} = 12$, $\mu_{F_2} = 100N$, and $\sigma_{F_2} = 10$. The basic probability assignments of the preset distributions are shown in Table 2. The synthesized uncertainty parameters are divided into 4×4 focal elements as shown in Fig 9. The other constraints are defined as $\sigma_s = 250\text{MPa}$, $u_{s,1} = 1.4\text{mm}$ (displacement of load point F_1), $u_{s,2} = 1.4\text{mm}$ (displacement of load point F_2), and $\bar{v}_{Mic} \leq 0.5$. The iteration processes are shown in Fig 10 and Fig 11. The design results are shown in Table 3 and Table 5. From the given results, the following points are summarized:

(1) Design results under a settled minimum length scale constraint ($b_{cons} = 0.05\text{mm}$) different target reliabilities have been shown in Table 3. The volume fractions of the entire structure under $R_{\text{arg}} = 0.90$, $R_{\text{arg}} = 0.95$, and $R_{\text{arg}} = 0.99$ are 16.35%, 16.89%, and 17.60% respectively. The relative volume fraction becomes higher when the target reliability increases, which implies that higher material assumption is needed to achieve higher reliability.

(2) The macro configurations in Table 3 show obvious differences while the micro configurations are similar. Since the micro sensitivities of the objective function are greater than the macro sensitivities, the cell configuration forms faster than the macro configuration. Meanwhile, the change of the cell configuration has less influence on the structural strength than the change of macro density, so the cell microstructures show little differences. In addition, the similarity of the micro configurations can also be attributed to the minimum length scale constraint, the cell volume constraint, and the initial material distribution. From the equivalent elastic matrices listed in Table 4, the values of the matrices have shown differences.

(3) Design results under different minimum length scale constraints and settled target reliability ($R_{\text{arg}} = 0.95$) are shown in Table 5. All the micro results have satisfied their respective minimum length scale constraint and the configurations of the cell microstructures have shown significant differences. The relative volume fractions of the results under $b_{\text{cons}} = 0.025\text{mm}$, $b_{\text{cons}} = 0.05\text{mm}$, and $b_{\text{cons}} = 0.1\text{mm}$ are 16.43%, 16.89%, and 28.58% respectively. The volume fraction becomes higher as b_{cons} increases, suggesting length scale control may lead to a weaker mechanical property.

(4) Design results under different focal element allocations are shown in Table 6. The values of the constraints are: $u_{s,1} = 1.4\text{mm}$, $u_{s,2} = 1.4\text{mm}$, $b_{\text{cons}} = 0.05\text{mm}$, $R_{\text{arg}} = 0.95$, and $v_{\text{cons}} = 0.5$. The macro design results under the three focal element allocations show distinctions, while the microstructure results are similar. Under the same constraints, the final design result of microstructure is almost not affected by focal element allocations due to the length scale constraint, which is also in line with the above conclusions. The differences in the macro design results reflect that the focal element allocations can greatly affect the iterative process. The final volume fraction decreases with the increase of the number of c_k , which indicates that more detailed focal element divisions can better evaluate the reliability and obtain better optimizing ability. The volume fractions of 4×4 (16.64%) and 5×5 (16.33%) cases are obviously less than that of 3×3 (17.37%), while the volume fraction of 4×4 and 5×5 show little difference. However, the 5×5 case takes about 1.5 times the solving time compared with 4×4 . Therefore, it is an important issue to properly balance the solving efficiency and optimization effect when arranging the allocation of the focal elements.

(5) Design results under different mesh divisions are shown in Table 7. The constraints of the three examples are the same as those in Table 6, and the focal element allocation is 4×4 . The final volume fractions of the three examples are very close, the microstructures are similar but the macrostructures show differences. The first two examples have different mesh numbers in the micro design domain. Although the final microstructure configurations are similar, the performance difference has affected the formation of the macrostructure. In the latter two examples, the mesh number of the macro design domain in the third example is changed, which leads to the reduction of the geometric size of the microstructure. Due to the same length scale constraint, the differences in microstructure configuration and properties affect the formation of the macrostructure. Therefore, the mesh-dependent phenomenon is normal in double-scale topology optimization, and the macro design domain is more sensitive since it is also affected

by the microstructure.

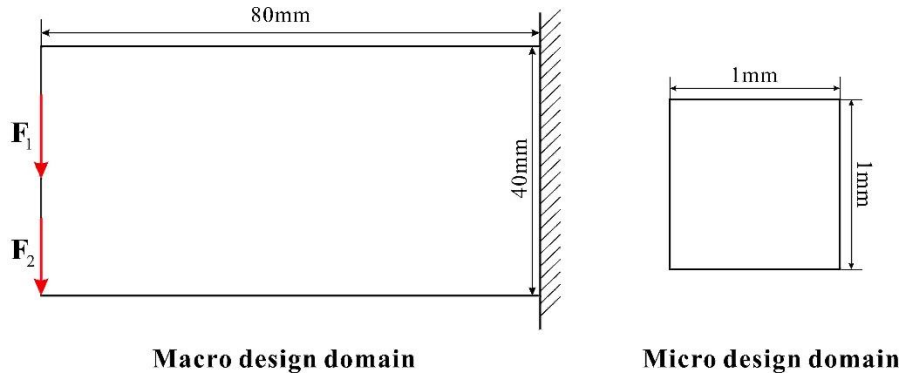
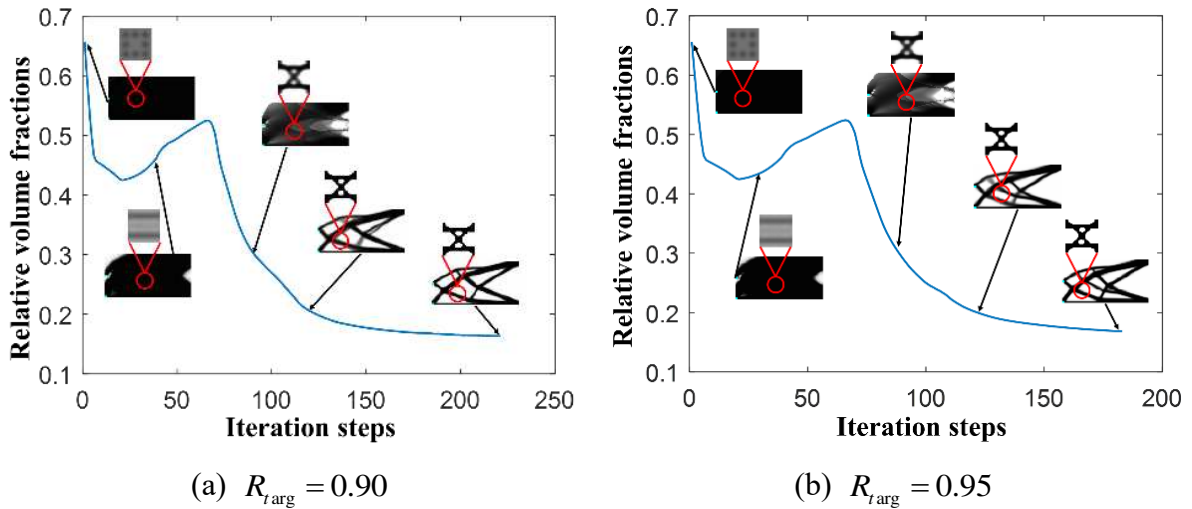
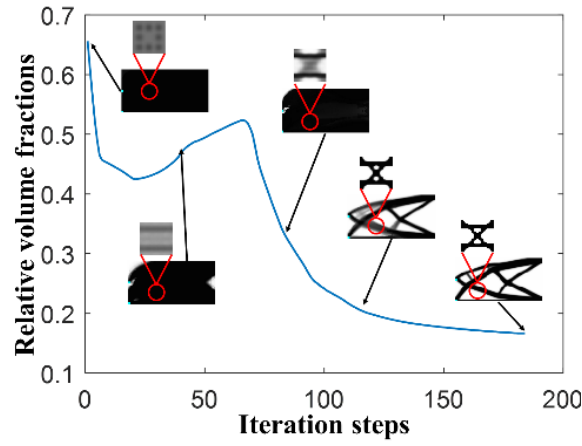


Fig 8 Design domains of the cantilever beam

F	f1	0.0002	0.0063	0.0073	0.0003
	f2	0.0063	0.1984	0.2297	0.0079
	f3	0.0073	0.2297	0.2659	0.0091
	f4	0.0003	0.0079	0.0091	0.0003
		e1	e2	e3	e4
		E			

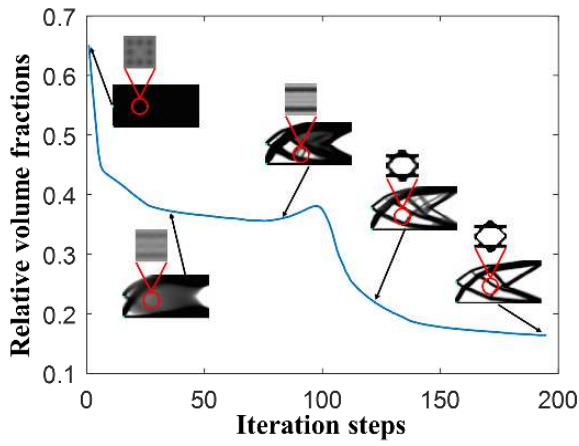
Fig 9 The focal elements of the synthesized uncertainty parameters



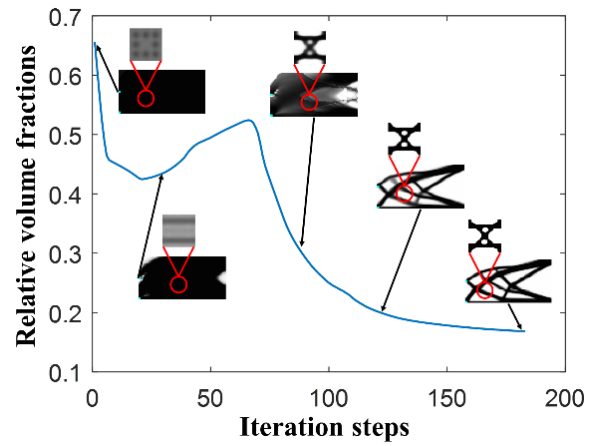


(c) $R_{\text{arg}} = 0.99$

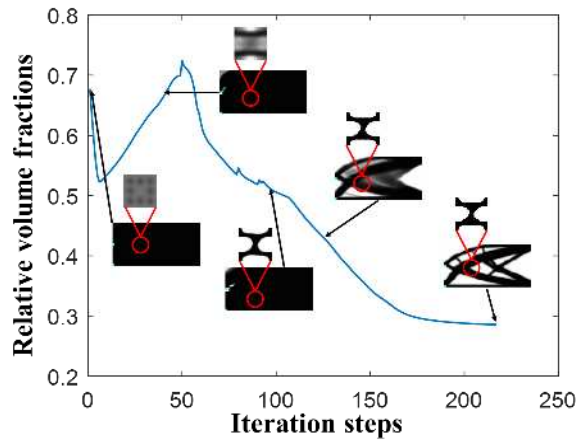
Fig 10 The iteration processes under different reliability constraints



(a) $b_{\text{cons}} = 0.025\text{mm}$



(b) $b_{\text{cons}} = 0.05\text{mm}$



(c) $b_{\text{cons}} = 0.1\text{mm}$

Fig 11 The iteration processes under different minimum length scale constraints

Table 2 The BPA of the preset uncertainty parameter distributions

E /MPa	F_1 /N	F_2 /N	m
[58e3,64e3]	[84,102]	[70,85]	0.08
[64e3,70e3]	[102,120]	[85,100]	0.38
[70e3,76e3]	[120,138]	[100,115]	0.44
[76e3,82e3]	[138,156]	[115,130]	0.1

Table 3 Design results under different reliability constraints

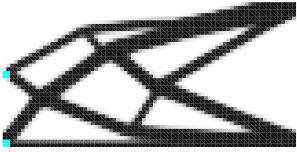
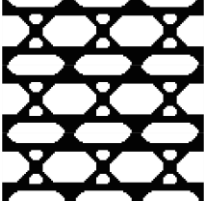
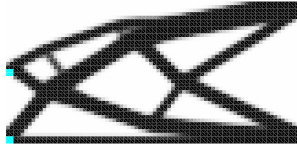
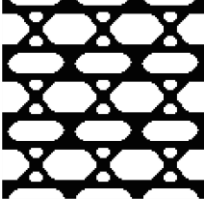
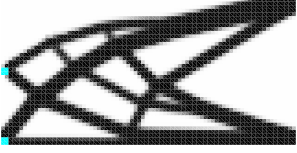
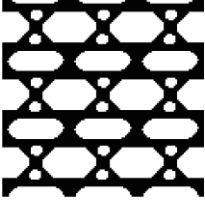
Design strategies	Macro configuration	Periodic arrangement of cells	The relative volume fraction	Convergence steps
$R_{targ} = 0.90$			16.35%	221
$R_{targ} = 0.95$			16.89%	183
$R_{targ} = 0.99$			17.60%	184

Table 4 Equivalent elastic matrices of the cell microstructures

R_{arg}	\mathbf{D}_H
0.90	$\begin{bmatrix} 5311.711 & 4001.078 & -677.150 \\ 4001.078 & 21239.865 & -552.254 \\ -677.150 & -552.254 & 4292.067 \end{bmatrix}$
0.95	$\begin{bmatrix} 5339.884 & 4025.685 & -665.839 \\ 4025.685 & 21370.826 & -531.529 \\ -665.839 & -531.529 & 4298.442 \end{bmatrix}$
0.99	$\begin{bmatrix} 5392.217 & 4031.195 & -607.960 \\ 4031.195 & 21243.665 & -518.255 \\ -607.960 & -518.255 & 4340.450 \end{bmatrix}$

Table 5 Design results under different minimum length scale constraints

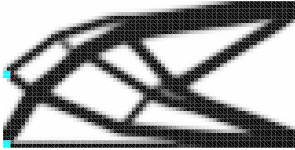
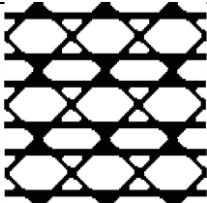
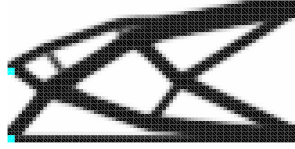
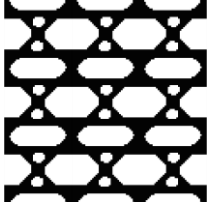
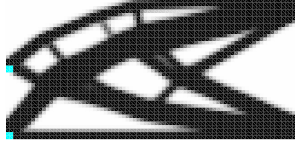
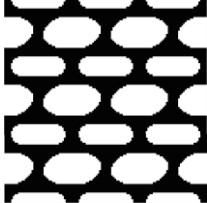
Design strategies	Macro configuration	Periodic arrangement of cells	The relative volume fraction	Convergence steps
$b_{\text{cons}} = 0.025\text{mm}$			16.43%	195
$b_{\text{cons}} = 0.05\text{mm}$			16.89%	183
$b_{\text{cons}} = 0.1\text{mm}$			28.58%	217

Table 6 Design results under different focal element allocations

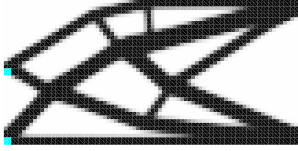
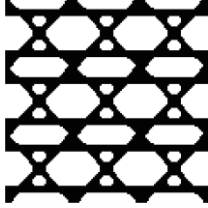
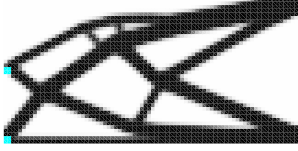
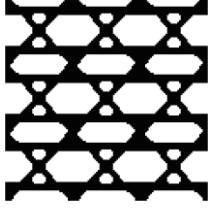
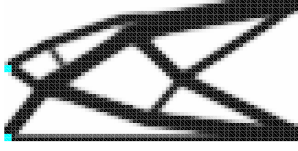
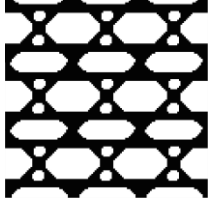
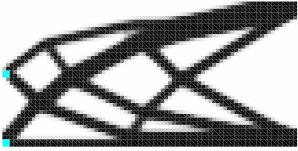
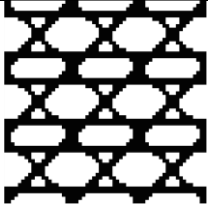
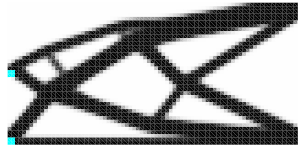
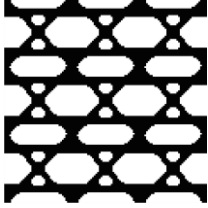

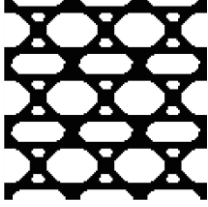
Focal element allocations	Macro configuration	Periodic arrangement of cells	The relative volume fraction	Convergence steps
3×3			17.37%	192
4×4			16.64%	187
5×5			16.33%	211

Table 7 Design results under different mesh divisions

Mesh division	Macro configuration	Periodic arrangement of cells	The relative volume fraction
Macro: 40×80 Micro: 20×20			16.69%
Macro: 40×80 Micro: 40×40			16.89%
Macro: 50×100 Micro: 40×40			16.73%

6.2 Optimization of an L-bracket

The optimization object in this example is an L-bracket fixed at the top side with a thickness of 1mm and a concentrated force F imposed on the top right corner as shown in Fig 12. The macro domain is divided into 3127 finite elements by $1\text{mm} \times 1\text{mm}$ four-node plane elements. The micro design domain is defined as a cell of the macro domain with a geometrical dimension of $1\text{mm} \times 1\text{mm}$. The micro design domain is divided into 1600 finite elements by $0.025\text{mm} \times 0.025\text{mm}$ four-node plane elements. The optimization aims at minimizing the volume fraction of the entire structure under the constraint of the global stress reliability, local displacement, and cell volume fraction. The external load F and Young's modulus E of the material are defined as uncertainty parameters with normal distributions. The expectation of the external load F is $\mu_F = 100\text{N}$ and the standard deviation is $\sigma_F = 15$. The expectation of Young's modulus E is $\mu_E = 70\text{e}3\text{ MPa}$ and the standard deviation is $\sigma_E = 4$. In order to contain more information about the distribution of the uncertainty parameters, the uncertainty parameter intervals are chosen as $[\mu - 3\sigma, \mu + 3\sigma]$. The uncertainty parameters intervals are divided into 4×4 focal elements as shown in Fig 13. The allowable value of the global condensed stress σ_{PN} is 100MPa and the cell volume fraction constraint is $\bar{v}_{Mic} \leq 0.5$. The local displacement constraint is imposed on the loading point and the constraint value is $u_{cons} = 1.5\text{mm}$.

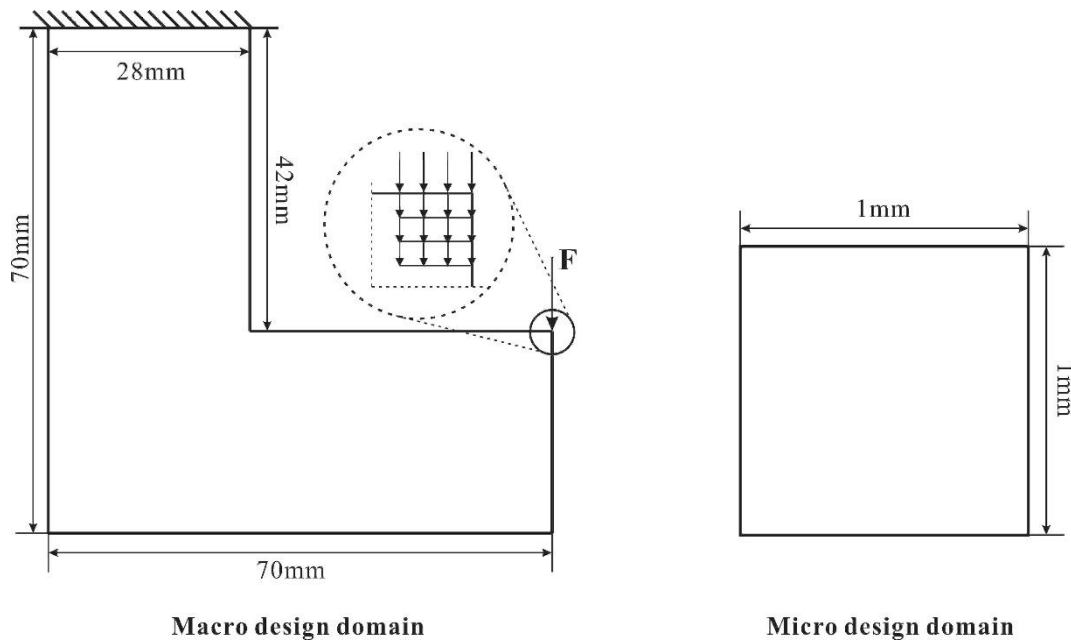


Fig 12 Design domains of the L-bracket

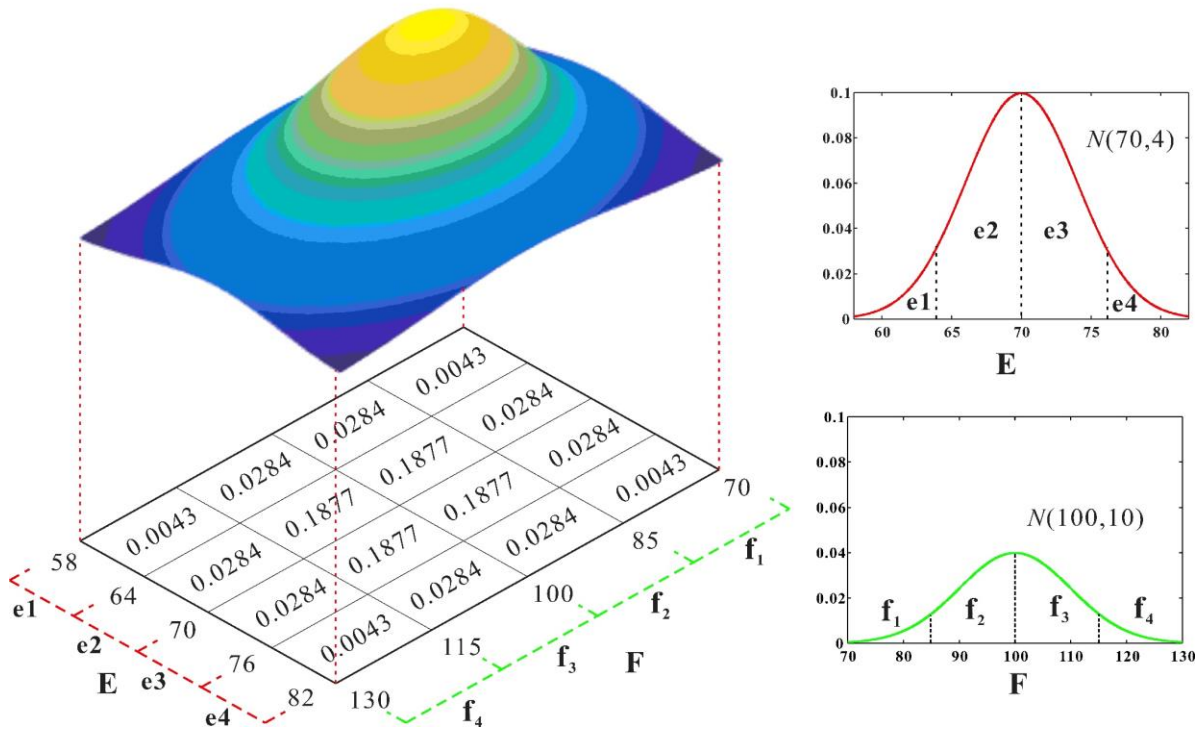


Fig 13 The focal elements of the uncertainty parameters

The design results under different reliability constraints ($R_{\text{target}} = 0.90$, $R_{\text{target}} = 0.95$, and $R_{\text{target}} = 0.99$) and different minimum length scale constraints ($b_{\text{cons}} = 0.04\text{mm}$, $b_{\text{cons}} = 0.06\text{mm}$, and $b_{\text{cons}} = 0.08\text{mm}$) are shown in Table 8 and Table 9. The iteration processes are shown in Fig 14 and Fig 15. According to the results presented, the following conclusions are summarized:

(1) As shown in Table 8, the volume fractions of the design results under $R_{\text{target}} = 0.90$, $R_{\text{target}} = 0.95$, and $R_{\text{target}} = 0.99$ are 0.2079, 0.2086, and 0.2150 respectively. Higher target reliability will lead to a higher volume fraction, implying a larger material cost is needed to realize higher reliability. In addition, the final reliabilities of the three results have all achieved $R = 1$. However, due to the reliability constraint effect in the optimization process, the volume fraction of the design result under a high reliability target tends to be higher.

(2) The cell configurations in Table 8 show significant differences and have satisfied the corresponding minimum length scale constraint ($b_{\text{cons}} = 0.04\text{mm}$). The differences in the cell configuration indicate that the reliability constraints may affect the formation of the cell microstructure. According to the periodic arrangement of the cell microstructure, the connectivity between the cell microstructures is well maintained, which can meet the

requirements of practical manufacturing.

(3) The design results under different minimum length scale constraints and $R_{\text{arg}} = 0.99$ are shown in Table 9. It can be observed that the cell microstructures have shown differences and have satisfied respective length scale constraints. Meanwhile, the length scale of the solid part and holes become larger as the minimum length scale constraint increases. The entire volume fractions of $b_{\text{cons}} = 0.04\text{mm}$, $b_{\text{cons}} = 0.06\text{mm}$, and $b_{\text{cons}} = 0.08\text{mm}$ are 0.2150, 0.2083, and 0.2763 while the cell volume fractions are 0.4028, 0.4829, and 0.4856. An oscillating appears in the iteration curve in Fig 15(b). Since the stress constraint in the optimization model is greatly affected by the local stress, the local stress concentration is likely to lead to an abrupt change of the stress value. In addition, the oscillation happens at the stage when the microstructure changes violently. The equivalent properties also change violently at this stage, which may lead to a stress jump at the macro level. The iteration can jump out of the oscillation after the microstructure changes tend to be stable.

(4) It can be observed in Fig 14(c) and Fig 15(a) that there are disconnected materials in the cell microstructures. The periodic arrangement of these microstructures reveals that these disconnected materials can actually be connected to adjacent cells as shown in Table 5 and Table 8. The periodic microstructure assumption (periodic boundary conditions) of the homogenization theory allows such cells. However, such suspended materials still exist at the edges of the macrostructure. In these cases, a small amount of auxiliary material may be needed to support these suspended materials for connectivity.

(5) Table 10 lists a group of mono-scale design results under different target reliabilities. When the target reliabilities are taken as 0.90, 0.95, and 0.99, no convergence results are obtained because the stress reliability constraints cannot be satisfied throughout the iteration. By comparing with Table 8, it can be found that the volume fraction of mono-scale design results is still larger than the three examples in Table 8 even after the reliability requirement is relaxed to 0.5. Such a phenomenon indicates that the double-scale model is undoubtedly advantageous for the proposed weight-reducing optimization problem. Although the solving efficiency of double-scale TO is much lower than that of mono-scale TO, double-scale TO has a larger design space and can search for feasible solutions in a wider range.

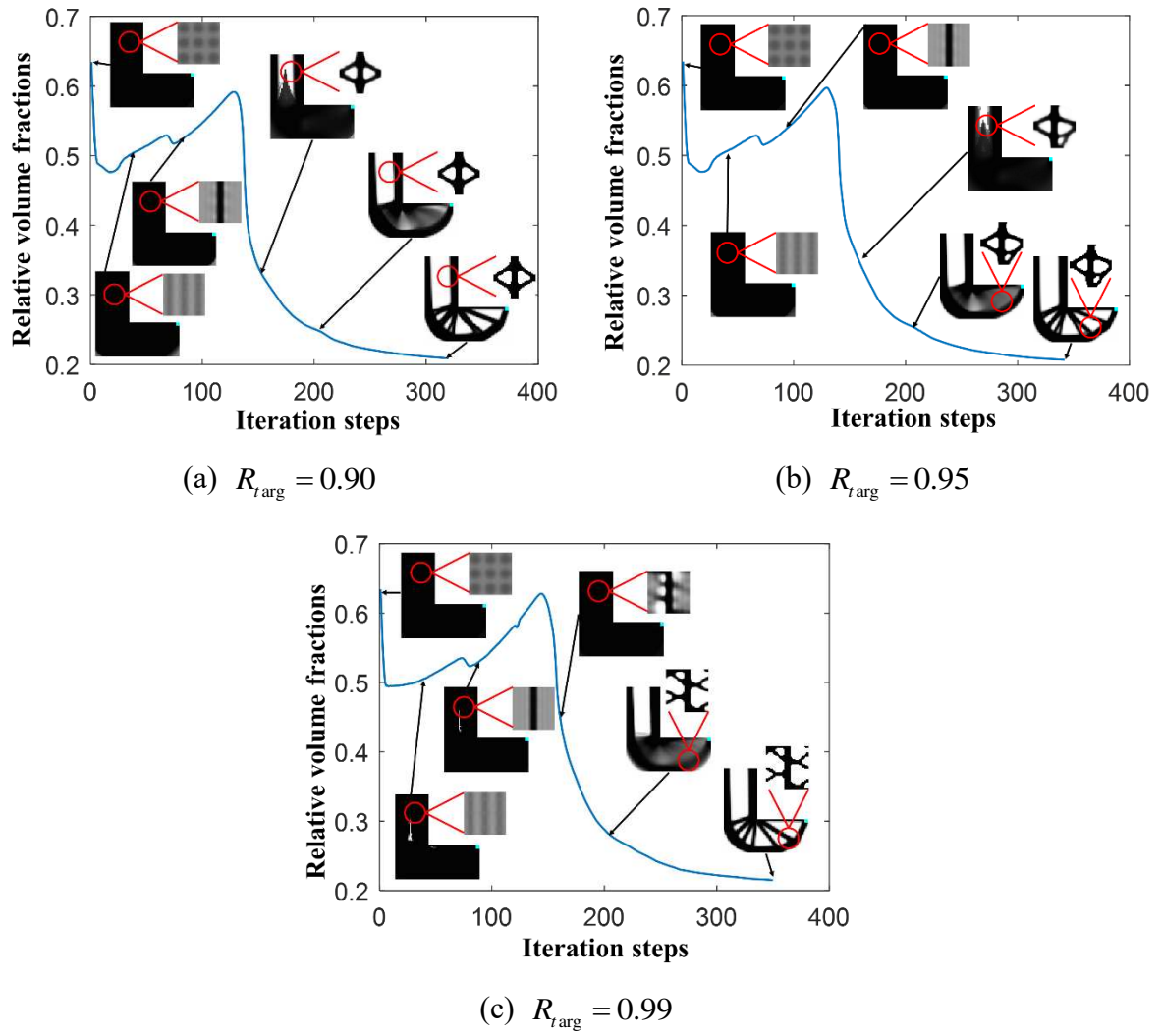
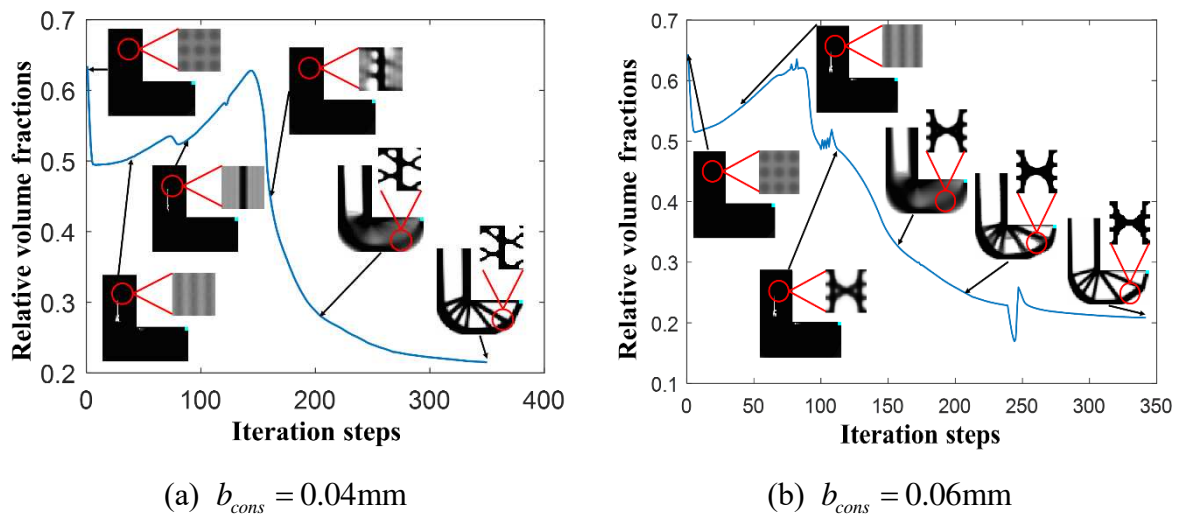


Fig 14 The iteration processes under different reliability constraints



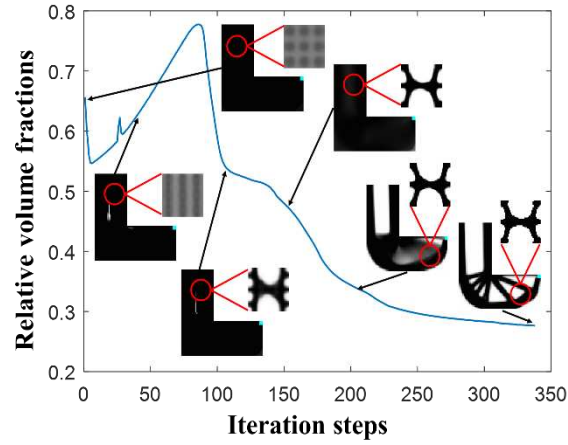

 (c) $b_{cons} = 0.08\text{mm}$

Fig 15 The iteration processes under different minimum length scale constraints

Table 8 Design results under different reliability constraints

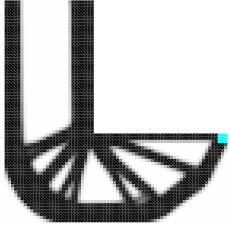
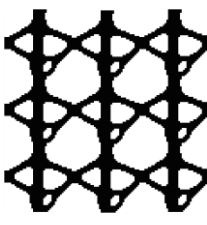
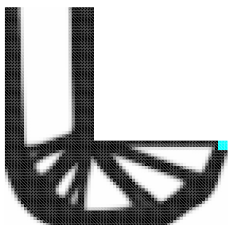

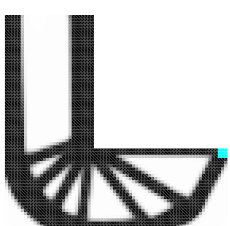
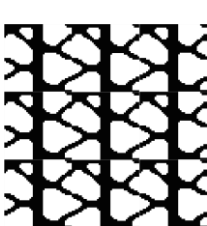
Design strategies	Macro configuration	Periodic arrangement of cells	The relative volume fraction	Convergence steps
$R_{target} = 0.90$			20.79%	342
$R_{target} = 0.95$			20.86%	320
$R_{target} = 0.99$			21.50%	350

Table 9 Design results under different minimum length scale constraints

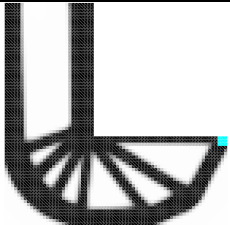

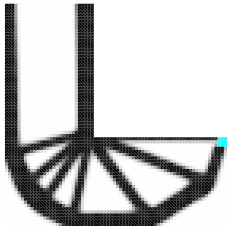
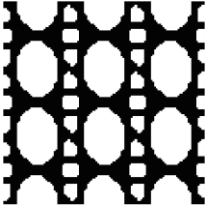
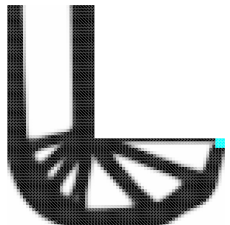
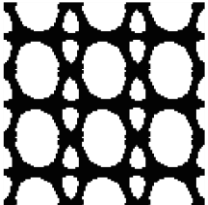
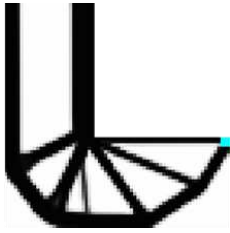
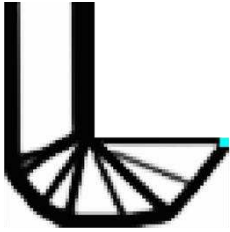
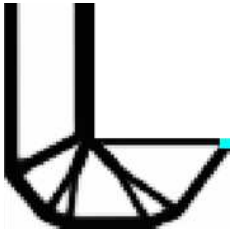
Design strategies	Macro configuration	Periodic arrangement of cells	The relative volume fraction	Convergence steps
$b_{cons} = 0.04\text{mm}$			21.50%	350
$b_{cons} = 0.06\text{mm}$			20.83%	343
$b_{cons} = 0.08\text{mm}$			27.63%	339

Table 10 Mono-scale design results under different reliability constraints

Design strategies	Macro configuration	The relative volume fraction	Convergence steps
$R_{targ} = 0.99$		Not converged	
$R_{targ} = 0.95$		Not converged	
$R_{targ} = 0.90$		Not converged	
$R_{targ} = 0.70$		42.28%	277
$R_{targ} = 0.60$		41.72%	166
$R_{targ} = 0.50$		37.25%	172

6.3 Optimization of an aircraft mid-wing rib

The third example is the topological design of an aircraft mid-wing rib (NACA 23016) under a series of boundary and loading conditions as shown in Fig 16. The macro design domain is divided by $1\text{mm} \times 1\text{mm}$ 4-node plane element. The micro design domain is an element of the macro design domain and is divided into 1600 4-node plane elements. Young's modulus of the material and external loads are uncertainty parameters. It is assumed that the uncertainty parameters submit to normal distributions and the loads fluctuate synchronously in the following examples. In addition, the range of the material and loading uncertainty parameters are chosen as $[\mu - 3\sigma, \mu + 3\sigma]$ and divided into 4×4 focal elements as shown in Fig 17. All the local displacement constraints are imposed on the loading points in the following four cases, and the number subscripts of u_{cons} denote corresponding loads. Case 1 and case 3 consider

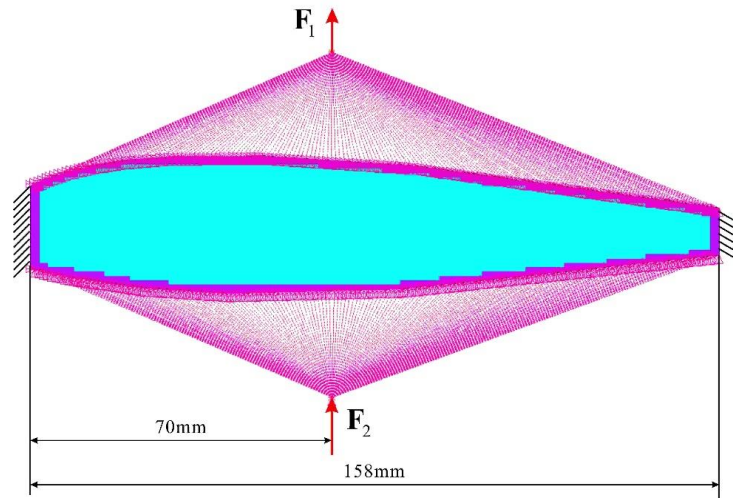
conventional boundary conditions of a wing rib. Case 2 and case 4 simulate the test state of a wing rib with attack angles.

In the first case, the left and right sides of the rib are fixed and two multi-point constraints are established with the top and bottom airfoils respectively as the loading points as shown in Fig 16(a). The normal distribution parameters are defined as: $\mu_E = 70e3$ MPa , $\sigma_E = 4$, $\mu_{F_1} = 600$ N , $\sigma_{F_1} = 40$, $\mu_{F_2} = 300$ N , and $\sigma_{F_2} = 10$. The allowable value of the global condensed stress σ_{PN} is 250MPa and the target reliability is 0.99. The other constraints are defined as $\bar{v}_{Mic} \leq 0.5$, $u_{cons} = 0.16$ mm , and $b_{cons} = 0.075$ mm . The iteration process and design result are shown in Fig 18(a).

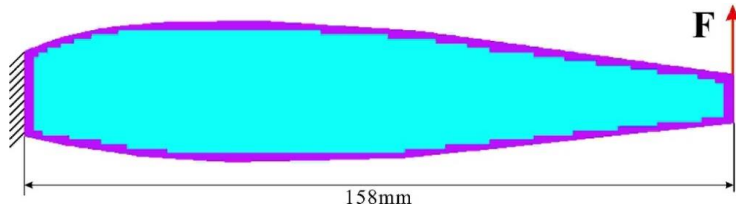
The second case is a wing rib fixed at the left side with a concentrated force imposed on the top right corner as shown in Fig 16(b). The normal distribution parameters are defined as: $\mu_E = 70e3$ MPa , $\sigma_E = 4$, $\mu_F = 100$ N , and $\sigma_F = 10$. The allowable value of the global condensed stress σ_{PN} is 200MPa and the target reliability is 0.95. The other constraints are defined as $\bar{v}_{Mic} \leq 0.5$, $u_{cons} = 6$ mm , and $b_{cons} = 0.08$ mm . The iteration process and design result are shown in Fig 18(b).

In the third case, the left and right side of the rib is fixed and 4 concentrated forces are imposed on the top and bottom airfoils as shown in Fig 16(c). The normal distribution parameters are defined as: $\mu_E = 70e3$ MPa , $\sigma_E = 4$, $\mu_{F_1} = 200$ N , $\sigma_{F_1} = 40/3$, $\mu_{F_2} = 100$ N , $\sigma_{F_2} = 20/3$, $\mu_{F_3} = 200$ N , $\sigma_{F_3} = 40/3$, $\mu_{F_4} = 100$ N , and $\sigma_{F_4} = 20/3$. The allowable value of the global condensed stress σ_{PN} is 250MPa and the target reliability is 0.95. The other constraints are defined as $\bar{v}_{Mic} \leq 0.5$, $u_{cons,1} = 2$ mm , $u_{cons,2} = 2$ mm , $u_{cons,3} = 1.8$ mm , $u_{cons,4} = 1.8$ mm and $b_{cons} = 0.05$ mm . The iteration process and design result are shown in Fig 18(c).

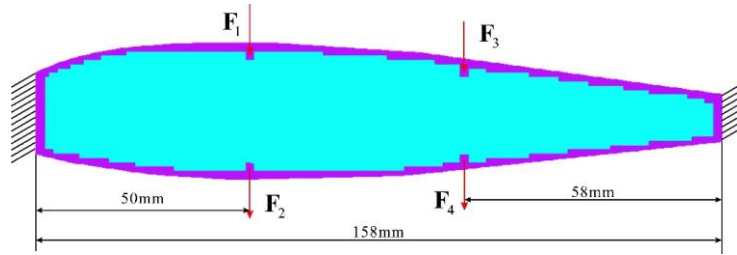
In the fourth case, the left side of the rib is fixed and two multi-point constraints are established with the top and bottom airfoils respectively as the loading points as shown in Fig 16(d). The normal distribution parameters are defined as: $\mu_E = 70e3$ MPa , $\sigma_E = 4$, $\mu_{F_1} = 300$ N , $\sigma_{F_1} = 20$, $\mu_{F_2} = 200$ N , and $\sigma_{F_2} = 40/3$. The allowable value of the global condensed stress σ_{PN} is 250MPa and the target reliability is 0.95. The other constraints are defined as $\bar{v}_{Mic} \leq 0.5$, $u_{cons,1} = 5.5$ mm , $u_{cons,2} = 5$ mm , and $b_{cons} = 0.05$ mm . The iteration process and design result are shown in Fig 18(d).



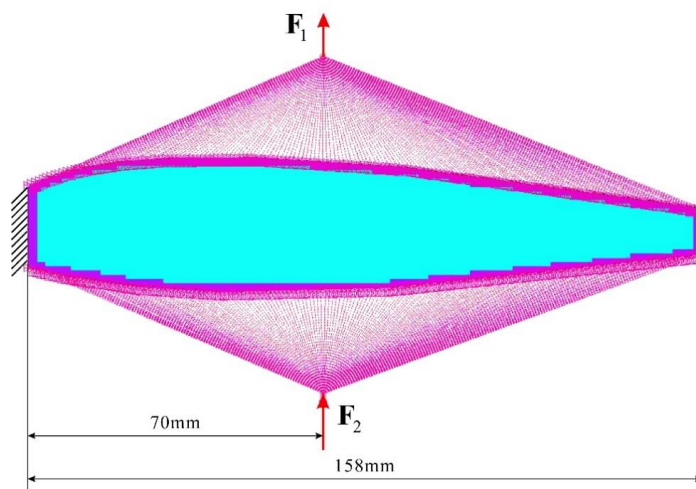
(a) Case 1



(b) Case 2



(c) Case 3



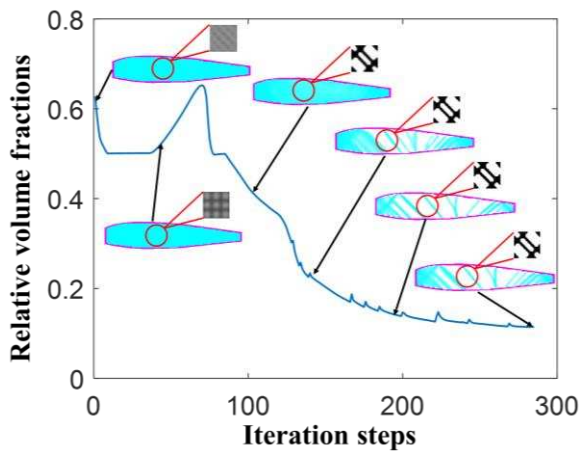
(d) Case 4

Fig 16 Boundary and loading conditions of the wing rib

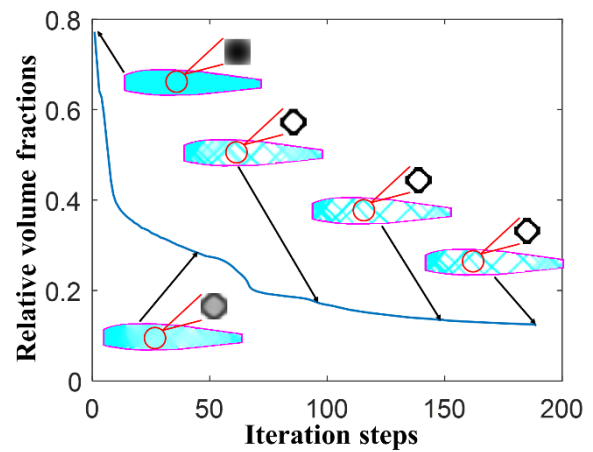
F	f4	0.0043	0.0284	0.0284	0.0043
	f3	0.0284	0.1877	0.1877	0.0284
	f2	0.0284	0.1877	0.1877	0.0284
	f1	0.0043	0.0284	0.0284	0.0043
		e1	e2	e3	e4
		E			

Fig 17 Focal elements of the uncertainty parameters

The design results of the four working conditions are shown in Table 11. The cell microstructures have satisfied their minimum length scale constraints and maintained good continuity. The results under several working conditions converge stably, which proves that the proposed method is suitable for different boundary and loading conditions. In some cases, gray units appear on the left or right sides of the macro configuration, which can be attributed to boundary conditions, loading mode, and the definition of the non-design domain. To reduce gray units, applying density projection to the macro design domain is also worth trying.



(a) Case 1



(b) Case 2

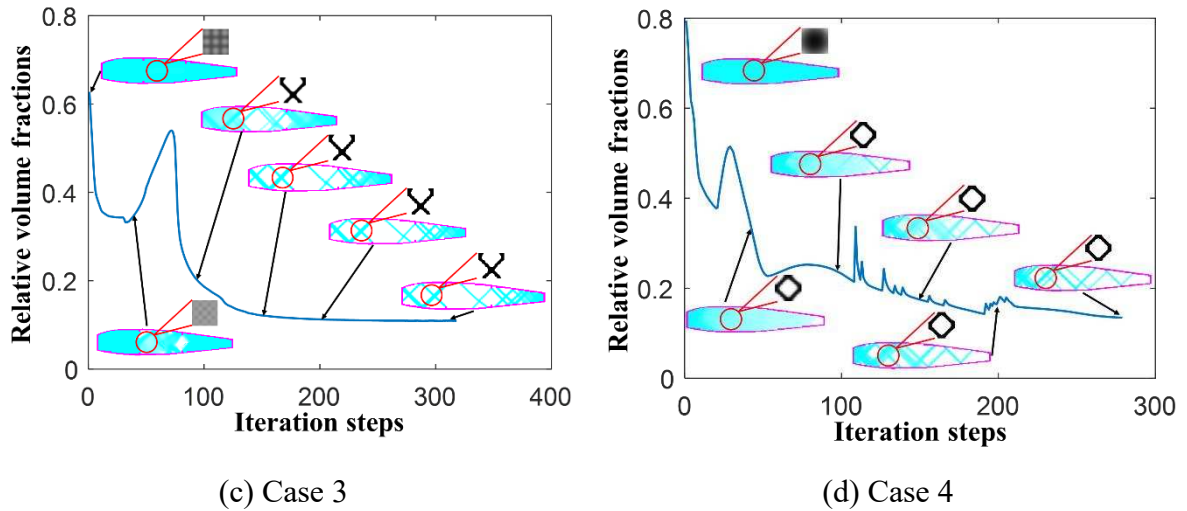
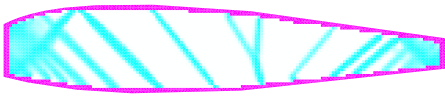
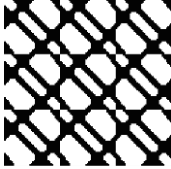

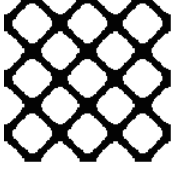






Fig 18 Iteration processes of the four working conditions

Table 11 Design results under different working conditions

Working condition	Macro configuration	Periodic arrangement of cells	The relative volume fraction	Convergence steps
Case 1			11.65%	299
Case 2			12.26%	189
Case 3			10.98%	318
Case 4			13.46%	279

7 Conclusions

A double-scale topology optimization strategy considering minimum length scale control, local displacement constraint, and the global stress reliability constraint based on the evidence theory is proposed in this paper. In the optimization framework, the evidence theory is

introduced to evaluate global stress failure probability with respect to uncertainty factors, and a density projection method is utilized to realize length scale control of the cell microstructure. Besides, some simplifications of the optimization procedure are discussed to economize computational consumption. Three numerical examples are presented to illustrate the effect of the proposed optimization framework.

In this paper, the evidence theory is introduced into the multi-scale continuum reliability topology optimization model, and the relative reliability index is constructed as a smoothed function to fit the gradient algorithm. In addition, a gradually changing smooth parameter is used in the reliability index to improve the iteration stability. Evidence theory may better evaluate structural reliability when there are multi-source uncertainty parameter inputs. Currently, there are few related studies on multi-scale continuum topology optimization. This study provides a complementary attempt in this field.

There are still some regrets in this study: The division of the focal elements is not elaborate enough due to the limitation of computing capacity. In addition, the initial material distribution of cells affects the final configuration greatly. In fact, an appropriate initial distribution may greatly promote optimization convergence, and an improper one may cause divergence. In conclusion, there is still room for improvement for the proposed method.

Acknowledgments

The authors would like to thank National Nature Science Foundation of China (12072007), the EU Marie Skłodowska-Curie Individual Fellowships (H2020-MSCA-IF-2020: 101025743-ROFiDMS), the Ningbo Nature Science Foundation (202003N4018), the Aeronautical Science Foundation of China (20182951014), the Defense Industrial Technology Development Program (JCKY2019205A006, JCKY2019209C004, JCKY2018601B001), and Beijing Advanced Discipline Center for Unmanned Aircraft System for the financial supports. Besides, the authors wish to express their many thanks to the reviewers for their useful and constructive comments.

Declarations

Compliance with ethical standards

Conflict of interest: The author declares that he has no conflict of interest with others.

Replication of Results: In this work, The basic codes for the evidence theory, the reliability-oriented design sensitivity analyses, and the numerical results presented are available from the author on reasonable request.

References

- [1] M.P. Bendsøe, N. Kikuchi (1988) Generating optimal topologies in structural design using a homogenization method. *Computer Methods in Applied Mechanics and Engineering* 71: 197-224. [https://doi.org/10.1016/0045-7825\(88\)90086-2](https://doi.org/10.1016/0045-7825(88)90086-2)
- [2] M.P. Bendsøe (1989) Optimal shape design as a material distribution problem. *Structural optimization* 1: 193-202. <https://doi.org/10.1007/BF01650949>
- [3] M. Bendsøe, O. Sigmund (1999) Material interpolation schemes in topology optimization. *Archive of Applied Mechanics* 69: 635-654. <https://doi.org/10.1007/s004190050248>
- [4] G.I.N. Rozvany, M. Zhou, T. Birker (1992) Generalized shape optimization without homogenization. *Structural Optimization* 4: 250-252. <https://doi.org/10.1007/BF01742754>
- [5] Y. Xie, G. Steven (1993) A Simple Evolutionary Procedure for Structural Optimization. *Computers & Structures* 49: 885-896. [https://doi.org/10.1016/0045-7949\(93\)90035-C](https://doi.org/10.1016/0045-7949(93)90035-C)
- [6] X. Huang, Y. Xie (2010) A further review of ESO type methods for topology optimization. *Structural and Multidisciplinary Optimization* 41: 671-683. <https://doi.org/10.1007/s00158-010-0487-9>
- [7] J.A. Sethian, A. Wiegmann (2000) Structural Boundary Design via Level Set and Immersed Interface Methods. *Journal of Computational Physics* 163: 489-528. <https://doi.org/10.1006/jcph.2000.6581>
- [8] S. Osher, F. Santosa (2001) Level Set Methods for Optimization Problems Involving Geometry and Constraints: I. Frequencies of a Two-Density Inhomogeneous Drum. *Journal of Computational Physics* 171: 272-288. <https://doi.org/10.1006/jcph.2001.6789>
- [9] G. Allaire, F. Jouve, A.-M. Toader (2004) Structural optimization using sensitivity analysis and a level-set method. *Journal of Computational Physics* 194: 363-393. <https://doi.org/10.1016/j.jcp.2003.09.032>
- [10] L. Wang, L. Zeshang, B. Ni, K. Gu (2021) Non-probabilistic Reliability-based Topology Optimization (NRBTO) Scheme for Continuum Structures Based on the parameterized Level-Set method and Interval Mathematics. *Computer Methods in Applied Mechanics and Engineering* 373: 113477. <https://doi.org/10.1016/j.cma.2020.113477>
- [11] M. Bendsøe, O. Sigmund, *Topology Optimization: Theory, Method and Applications*, 2003.
- [12] G. Sved, Z. Ginos (1968) Structural optimization under multiple loading. *International Journal of Mechanical Sciences - INT J MECH SCI* 10: 803-805. [https://doi.org/10.1016/0020-7403\(68\)90021-0](https://doi.org/10.1016/0020-7403(68)90021-0)
- [13] G. Cheng (1997) ϵ -Relaxed approach in structural topology optimization. *Structural Optimization* 13: 258-266. <https://doi.org/10.1007/BF01197454>
- [14] G. Rozvany, J. Sobieszczanski-Sobieski (1992) New optimality criteria methods - Forcing uniqueness of the adjoint strains by corner-rounding at constraint intersections. *Structural Optimization* 4. <https://doi.org/10.1007/BF01742752>
- [15] M. Bruggi (2008) On an alternative approach to stress constraints relaxation in topology optimization. *Structural and Multidisciplinary Optimization* 36: 125-141. <https://doi.org/10.1007/s00158-007-0203-6>
- [16] P. Duysinx, O. Sigmund, New developments in handling stress constraints in optimal material distribution, 1998. <https://doi.org/10.2514/6.1998-4906>
- [17] R.-J. Yang, C.-J. Chen (1996) Stress-based topology optimization. *Structural and Multidisciplinary Optimization* 12: 98-105. <https://doi.org/10.1007/BF01196941>
- [18] X. Haijun, L. Wang, Y. Liu (2020) Uncertainty-oriented topology optimization of interval parametric structures with local stress and displacement reliability constraints. *Computer Methods in Applied Mechanics and Engineering* 358: 112644. <https://doi.org/10.1016/j.cma.2019.112644>
- [19] O. Sigmund (1994) Materials with prescribed constitutive parameters: An inverse

- homogenization problem. *International Journal of Solids and Structures* 31: 2313-2329. [https://doi.org/10.1016/0020-7683\(94\)90154-6](https://doi.org/10.1016/0020-7683(94)90154-6)
- [20] S. Watts, W. Arrighi, J. Kudo, D. Tortorelli, D. White (2019) Simple, accurate surrogate models of the elastic response of three-dimensional open truss micro-architectures with applications to multiscale topology design. *Structural and Multidisciplinary Optimization* 60. <https://doi.org/10.1007/s00158-019-02297-5>
- [21] P. Zhang, J. Toman, Y. Yu, E. Biyikli, M. Kirca, M. Chmielus, A. To (2015) Efficient Design-Optimization of Variable-Density Hexagonal Cellular Structure by Additive Manufacturing: Theory and Validation. *Journal of Manufacturing Science and Engineering* 137: 021004. <https://doi.org/10.1115/1.4028724>
- [22] D. White, W. Arrighi, J. Kudo, S. Watts (2018) Multiscale topology optimization using neural network surrogate models. *Computer Methods in Applied Mechanics and Engineering* 346. <https://doi.org/10.1016/j.cma.2018.09.007>
- [23] C. Wang, X. Gu, J. Zhu, H. Zhou, S. Li, W. Zhang (2020) Concurrent design of hierarchical structures with three-dimensional parameterized lattice microstructures for additive manufacturing. *Structural and Multidisciplinary Optimization* 61. <https://doi.org/10.1007/s00158-019-02408-2>
- [24] C. Imediegwu, R. Murphy, Santer, R. Hewson (2019) Multiscale structural optimization towards three-dimensional printable structures. *Structural and Multidisciplinary Optimization* 60. <https://doi.org/10.1007/s00158-019-02220-y>
- [25] J. Zhao, H. Yoon, B.D. Youn (2019) Concurrent topology optimization with uniform microstructure for minimizing dynamic response in the time domain. *Computers & Structures* 222: 98-117. <https://doi.org/10.1016/j.compstruc.2019.07.008>
- [26] J. Deng, W. Chen (2017) Concurrent topology optimization of multiscale structures with multiple porous materials under random field loading uncertainty. *Structural and Multidisciplinary Optimization* 56. <https://doi.org/10.1007/s00158-017-1689-1>
- [27] Y.J.G.X.C. G (2016) Multi-scale concurrent material and structural design under mechanical and thermal loads. *Computational Mechanics* 57: 446. <https://doi.org/10.1007/s00466-015-1255-x>
- [28] S. Das, A. Sutradhar (2020) Multi-physics topology optimization of functionally graded controllable porous structures: Application to heat dissipating problems. *Materials & Design* 193: 108775. <https://doi.org/10.1016/j.matdes.2020.108775>
- [29] Y. Zhang, M. Xiao, H. Li, L. Gao, S. Chu (2018) Multiscale concurrent topology optimization for cellular structures with multiple microstructures based on ordered SIMP interpolation. *Computational Materials Science* 155: 74-91. <https://doi.org/10.1016/j.commatsci.2018.08.030>
- [30] J. Gao, Z. Luo, H. Li, L. Gao (2018) Topology optimization for multiscale design of porous composites with multi-domain microstructures. *Computer Methods in Applied Mechanics and Engineering* 344: 451-476. <https://doi.org/10.1016/j.cma.2018.10.017>
- [31] L. xu, G. Cheng (2018) Two-scale concurrent topology optimization with multiple micro materials based on principal stress orientation. *Structural and Multidisciplinary Optimization* 57. <https://doi.org/10.1007/s00158-018-1916-4>
- [32] Y. Ben-Haim (1994) A non-probability concept of reliability. *Structural Safety* 14: 227-245. [https://doi.org/10.1016/0167-4730\(94\)90013-2](https://doi.org/10.1016/0167-4730(94)90013-2)
- [33] L. Wang, Y. Liu, Y. Liu (2019) An inverse method for distributed dynamic load identification of structures with interval uncertainties. *Advances in Engineering Software* 131: 77-89. <https://doi.org/10.1016/j.advengsoft.2019.02.003>
- [34] C. Xiong, L. Wang, G. Liu, Q. Shi (2019) An iterative dimension-by-dimension method for structural interval response prediction with multidimensional uncertain variables. *Aerospace Science and Technology* 86. <https://doi.org/10.1016/j.ast.2019.01.032>

- [35] A. Dempster, Upper and Lower Probabilities Induced by a Multivalued Mapping, in, 2008, pp. 57-72. https://doi.org/10.1007/978-3-540-44792-4_3
- [36] A. Smith, G. Shafer (1976) A Mathematical Theory of Evidence. *Biometrics* 32: 703. <https://doi.org/10.2307/2529769>
- [37] H. Agarwal, J. Renaud, E. Preston, D. Padmanabhan (2004) Uncertainty quantification using evidence theory in multidisciplinary design optimization. *Reliability Engineering & System Safety* 85: 281-294. <https://doi.org/10.1016/j.res.2004.03.017>
- [38] H.R. Bae, R. Grandhi, R. Canfield (2004) An approximation approach for uncertainty quantification using evidence theory. *Reliability Engineering & System Safety* 86: 215-225. <https://doi.org/10.1016/j.res.2004.01.011>
- [39] M.J. Zhou (2006) A design optimization method using evidence theory. *J Mech des* 128: 1153-1161.
- [40] M. Vasile (2006) Robust Mission Design Through Evidence Theory and Multi-Agent Collaborative Search. *Annals of the New York Academy of Sciences* 1065: 152-173. <https://doi.org/10.1196/annals.1370.024>
- [41] J. Petersson, O. Sigmund (1998) Slope constrained topology optimization. *International Journal for Numerical Methods in Engineering* 41: 1417-1434. [https://doi.org/10.1002/\(SICI\)1097-0207\(19980430\)41:8<1417::AID-NME344>3.0.CO;2-N](https://doi.org/10.1002/(SICI)1097-0207(19980430)41:8<1417::AID-NME344>3.0.CO;2-N)
- [42] T. Bruns, D. Tortorelli (2001) Topology optimization of non-linear structures and compliant mechanisms. *Computer Methods in Applied Mechanics and Engineering* 190: 3443-3459. [https://doi.org/10.1016/S0045-7825\(00\)00278-4](https://doi.org/10.1016/S0045-7825(00)00278-4)
- [43] T. Poulsen (2003) A new scheme for imposing minimum length scale in topology optimization. *International Journal for Numerical Methods in Engineering* 57: 741-760. <https://doi.org/10.1002/nme.694>
- [44] J. Guest, J. Prevost, T. Belytschko (2004) Achieving minimum length scale in topology optimization using nodal design variable and projection functions. *International Journal for Numerical Methods in Engineering* 61: 238-254. <https://doi.org/10.1002/nme.1064>
- [45] O. Sigmund (2009) Manufacturing tolerant topology optimization. *Acta Mechanica Sinica - ACTA MECH SINICA* 25: 227-239. <https://doi.org/10.1007/s10409-009-0240-z>
- [46] W. Zhang, W. Zhong (2014) An explicit length scale control approach in SIMP-based topology optimization. *Computer Methods in Applied Mechanics and Engineering* 282. <https://doi.org/10.1016/j.cma.2014.08.027>
- [47] O. Amir, B. Lazarov (2018) Achieving stress-constrained topological design via length scale control. *Structural and Multidisciplinary Optimization* 58. <https://doi.org/10.1007/s00158-018-2019-y>
- [48] S. Chen, M. Wang, A.-q. Liu (2008) Shape feature control in structural topology optimization. *Computer-Aided Design* 40: 951-962. <https://doi.org/10.1016/j.cad.2008.07.004>
- [49] W. Zhang, W. Zhong (2014) Explicit feature control in structural topology optimization via level set method. *Computer Methods in Applied Mechanics and Engineering* 272. <https://doi.org/10.1016/j.cma.2014.01.010>
- [50] Q. Xia, T. Shi (2015) Constraints of distance from boundary to skeleton: For the control of length scale in level set based structural topology optimization. *Computer Methods in Applied Mechanics and Engineering* 295. <https://doi.org/10.1016/j.cma.2015.07.015>
- [51] C. Le, J. Norato, T. Bruns, C. Ha, D. Tortorelli (2010) Stress-based topology optimization for continua. *Structural and Multidisciplinary Optimization* 41: 605-620. <https://doi.org/10.1007/s00158-009-0440-y>
- [52] G. Rozvany, U. Kirsch (1995) Layout Optimization of Structures. *Appl. Mech. Rev.* 48. <https://doi.org/10.1115/1.3005097>
- [53] O. Sigmund, K. Maute (2013) Topology optimization approaches A comparative review. *Structural and Multidisciplinary Optimization* 48. <https://doi.org/10.1007/s00158-013-0978-6>

- [54] M. Ma, L. Wang (2021) Reliability-based Topology Optimization Framework of Two-dimensional Phononic Crystal Band-gap Structures Based on Interval Series Expansion and Mapping Conversion Method. *International Journal of Mechanical Sciences* 196: 106265. <https://doi.org/10.1016/j.ijmecsci.2020.106265>
- [55] K. Suzuki, N. Kikuchi (1991) A Homogenization method for shape and topology optimization. *Computer Methods in Applied Mechanics and Engineering* 93: 291-318. [https://doi.org/10.1016/0045-7825\(91\)90245-2](https://doi.org/10.1016/0045-7825(91)90245-2)
- [56] F. Wang, B. Lazarov, O. Sigmund (2011) On projection methods, convergence and robust formulations in topology optimization. *Structural and Multidisciplinary Optimization* 43: 767-784. <https://doi.org/10.1007/s00158-010-0602-y>
- [57] S. Liu, G. Cheng, Y. Gu, X. Zheng (2002) Mapping method for sensitivity analysis of composite material property. *Structural and Multidisciplinary Optimization* 24: 212-217. <https://doi.org/10.1007/s00158-002-0237-8>

Figure captions

Fig 1 The Gaussian points under the local coordinate

Fig 2 Double-scale topology optimization

Fig 3 Stress failure domain of the joint FOD

Fig 4 Estimation procedure of stress failure probability based on evidence theory

Fig 5 Partial curves of the hyperbolic tangent functions

Fig 6 Length scale control effect of three density projection designs

Fig 7 Procedure of optimization iteration

Fig 8 Design domains of the cantilever beam

Fig 9 The focal elements of the synthesized uncertainty parameters

Fig 10 The iteration processes under different reliability constraints

Fig 11 The iteration processes under different minimum length scale constraints

Fig 12 Design domains of the L-bracket

Fig 13 The focal elements of the uncertainty parameters

Fig 14 The iteration processes under different reliability constraints

Fig 15 The iteration processes under different minimum length scale constraints

Fig 16 Boundary and loading conditions of the wing rib

Fig 17 Focal elements of the uncertainty parameters

Fig 18 Iteration processes of the four working conditions

Table captions

Table 1 The computational consumption in each stage of iteration

Table 2 The BPA of the preset uncertainty parameter distributions

Table 3 Design results under different reliability constraints

Table 4 Equivalent elastic matrices of the cell microstructures

Table 5 Design results under different minimum length scale constraints

Table 6 Design results under different focal element allocations

Table 7 Design results under different mesh divisions

Table 8 Design results under different reliability constraints

Table 9 Design results under different minimum length scale constraints

Table 10 Mono-scale design results under different reliability constraints

Table 11 Design results under different working conditions